Revisiting global fossil fuel and biofuel emissions of ethane

Z. A. Tzompa-Sosa[1] iD, E. Mahieu[2] iD, B. Franco[2,3], C. A. Keller[4] iD, A. J. Turner[4], D. Helmig[5] iD, A. Fried[5] iD, D. Richter[5] iD, P. Weibring[5], J. Walega[5], T. I. Yacovitch[6] iD, S. C. Herndon[6], D. R. Blake[7], F. Hase[8], J. W. Hannigan[9] iD, S. Conway[10] iD, K. Strong[10], M. Schneider[8], and E. V. Fischer[1]

[1]Department of Atmospheric Science, Colorado State University, Fort Collins, Colorado, USA, [2]Institut d'Astrophysique et de Géophysique, Université de Liège, Quartier Agora, Liège, Belgium, [3]Institute for Energy and Climate Research: Troposphere, Forschungszentrum Jülich, Jülich, Germany, [4]School of Engineering and Applied Science, Harvard University, Cambridge, Massachusetts, USA, [5]Institute of Arctic and Alpine Research, University of Colorado Boulder, Boulder, Colorado, USA, [6]Center for Atmospheric and Environmental Chemistry, Aerodyne Research Inc., Billerica, Massachusetts, USA, [7]Department of Chemistry, University of California, Irvine, California, USA, [8]Institute of Meteorology and Climate Research (IMK-ASF), Karlsruhe Institute of Technology, Karlsruhe, Germany, [9]National Center for Atmospheric Research, Boulder, Colorado, USA, [10]Department of Physics, University of Toronto, Toronto, Ontario, Canada

Abstract Recent measurements over the Northern Hemisphere indicate that the long-term decline in the atmospheric burden of ethane (C_2H_6) has ended and the abundance increased dramatically between 2010 and 2014. The rise in C_2H_6 atmospheric abundances has been attributed to oil and natural gas extraction in North America. Existing global C_2H_6 emission inventories are based on outdated activity maps that do not account for current oil and natural gas exploitation regions. We present an updated global C_2H_6 emission inventory based on 2010 satellite-derived CH_4 fluxes with adjusted C_2H_6 emissions over the U.S. from the National Emission Inventory (NEI 2011). We contrast our global 2010 C_2H_6 emission inventory with one developed for 2001. The C_2H_6 difference between global anthropogenic emissions is subtle (7.9 versus 7.2 Tg yr^{-1}), but the spatial distribution of the emissions is distinct. In the 2010 C_2H_6 inventory, fossil fuel sources in the Northern Hemisphere represent half of global C_2H_6 emissions and 95% of global fossil fuel emissions. Over the U.S., unadjusted NEI 2011 C_2H_6 emissions produce mixing ratios that are 14–50% of those observed by aircraft observations (2008–2014). When the NEI 2011 C_2H_6 emission totals are scaled by a factor of 1.4, the Goddard Earth Observing System Chem model largely reproduces a regional suite of observations, with the exception of the central U.S., where it continues to underpredict observed mixing ratios in the lower troposphere. We estimate monthly mean contributions of fossil fuel C_2H_6 emissions to ozone and peroxyacetyl nitrate surface mixing ratios over North America of ~1% and ~8%, respectively.

1. Introduction

Ethane (C_2H_6) is a hydrocarbon emitted mainly during the production, processing, and transportation of natural gas, and it has been proposed as a tracer for fugitive emissions from natural gas production [*Schwietzke et al.*, 2014; *Swarthout et al.*, 2013; *Vinciguerra et al.*, 2015]. In locations with multiple methane (CH_4) sources (e.g., cows, oil and gas, rice production, and wetlands), C_2H_6 can be used as a tracer for fossil fuel CH_4 emissions [*McKain et al.*, 2015; *Roscioli et al.*, 2015]. Natural gas leakage contributes about ~60% of C_2H_6 emissions globally [*Xiao et al.*, 2008] and up to 70% in regions with active oil and gas development [*Gilman et al.*, 2013]. Other important sources of C_2H_6 are biomass burning and biofuel consumption (domestic wood fuels), and each of these sources is estimated to individually account for ~20% of global emissions [*Rudolph and Ehhalt*, 1981; *Singh and Zimmerman*, 1992; *Xiao et al.*, 2008; *Zimmerman et al.*, 1988]. Biogenic and oceanic emissions of C_2H_6 are considered negligible on a global scale [*Plass-Dülmer et al.*, 1995; *Rudolph*, 1995; *Zimmerman et al.*, 1988].

Ethane is one of the most abundant volatile organic compounds (VOCs) in the atmosphere after CH_4. Observed C_2H_6 mixing ratios near the surface range from ~0.2 ppbv over remote regions of the Southern Hemisphere [*Wofsy et al.*, 2012] and up to 1500 ppbv over oil and natural gas basins [*Gilman et al.*, 2013; *Helmig et al.*, 2014b; *Thompson et al.*, 2014]. The primary tropospheric sink of C_2H_6 is oxidation via reaction with hydroxyl radicals (OH). This loss pathway gives atmospheric C_2H_6 a strong seasonality and a seasonally dependent lifetime with a global annual average of ~2 months [*Rudolph and Ehhalt*, 1981]. Based upon an
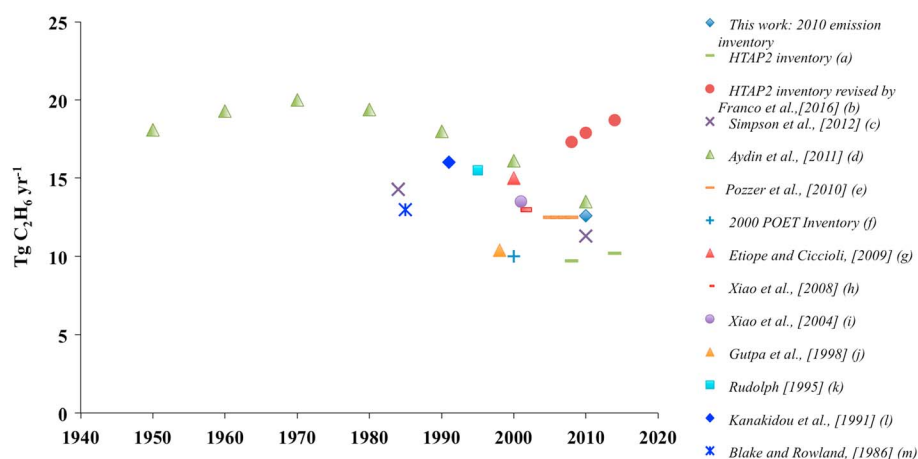
Figure 1. Estimated global annual emissions of C_2H_6 in Tg yr^{-1}. Total emissions correspond to the base year of each global estimate, if any, otherwise they correspond to the year they were published. (a) HTAP2 inventory for 2008 and 2014 as reported by *Franco et al.* [2016]. Total emissions from anthropogenic sources (7.5 Tg yr^{-1}), biomass burning (1.8–2.3 Tg yr^{-1}), and biogenic (0.4 Tg yr^{-1}). (b) HTAP2 global anthropogenic emissions for 2008 were doubled for all years prior to 2009, with increasing North American emissions after 2009. (c) Total emissions from fossil fuels (8.0–9.2 Tg yr^{-1}), biofuels (2.6 Tg yr^{-1}), and biomass burning (2.4–2.8 Tg yr^{-1}). (d) Emissions histories of total emissions from fossil fuels, biofuels and biomass burning. (e) Total emissions from anthropogenic (9.2 Tg yr^{-1}), biomass burning (2.8 Tg yr^{-1}), and oceanic (0.5 Tg yr^{-1}) sources. (f) POET inventory for 2000 as reported by *Etiope and Ciccioli* [2009]. Total emissions from anthropogenic (5.7 Tg yr^{-1}), forest-savanna burning (2.6 Tg yr^{-1}), biogenic (0.8 Tg yr^{-1}), and ocean (0.8 Tg yr^{-1}). (g) Total emissions from POET Inventory base year 2000, with additional geologic emissions (2–4 Tg yr^{-1}). (h) Total emissions from fossil fuels (8.0 Tg yr^{-1}), biofuels (2.6 Tg yr^{-1}), and biomass burning (2.4 Tg yr^{-1}). (i) Total emissions reported by *Xiao et al.* [2008]. (j) As reported by *Gupta et al.* [1998]. (k) As reported by *Rudolph* [1995]. (l) As reported by *Kanakidou et al.* [1991]. (m) As reported by *Blake and Rowland* [1986].

approximate CH_4/C_2H_6 ratio of 2000 ppbv/2 ppbv and their relative reaction rates with OH, C_2H_6 can make an instantaneous contribution of 4–7% of the total OH loss for these two species combined (depending upon temperature and the specific enhancements encountered). Strong increases in C_2H_6 relative to CH_4 have been found in shale gas-producing areas such as the Bakken [*Kort et al.*, 2016], and thus, the contribution of C_2H_6 to OH reactivity may become more important in the future. Other minor tropospheric sinks of C_2H_6 include reaction with chlorine (Cl) radicals [*Aikin et al.*, 1982] and loss via transport into the stratosphere [*Rudolph*, 1995]. The relatively long lifetime of C_2H_6 allows it to be subject to long-range transport and to be relatively well mixed in the troposphere within each hemisphere. Since most of the anthropogenic C_2H_6 sources are concentrated in the Northern Hemisphere, and its lifetime is shorter than the interhemispheric exchange rate, there is a strong hemispheric gradient in C_2H_6 [*Aydin et al.*, 2011; *Helmig et al.*, 2016; *Pozzer et al.*, 2010; *Rudolph*, 1995; *Simpson et al.*, 2012].

Ethane is a precursor of carbon monoxide (CO), ozone (O_3), and peroxyacetyl nitrate (PAN) in the troposphere [*Aikin et al.*, 1982]. C_2H_6 degradation can lead to the production of O_3 via two pathways: (1) C_2H_6 oxidation by OH radicals in the presence of nitrogen oxide radicals ($NO_x = NO + NO_2$) and (2) by serving as a precursor for PAN. PAN acts as a reservoir for NO_x [*Aikin et al.*, 1982; *Fischer et al.*, 2014], and its thermal decomposition over remote areas can efficiently produce O_3 [*Fischer et al.*, 2011]. C_2H_6 impacts the distribution of several atmospherically relevant species due to its main removal process via reaction with OH radicals [*Blake and Rowland*, 1986]; however, this impact is smaller compared to other species such as CO, CH_4, and isoprene.

Global C_2H_6 emissions have significantly changed over the last century. The recent literature is summarized in Figure 1. Briefly, measurements in firn air from Greenland and Antarctica show rising concentrations of C_2H_6 starting in the 1900s and peaking in the 1970s, followed by a decrease that lasted until the late 2000s [*Aydin et al.*, 2011; *Helmig et al.*, 2014a]. The decrease in C_2H_6 between 1970 and 2006 observed by *Aydin et al.* [2011] was attributed to a reduction in fugitive emissions from the fossil fuel sector. *Simpson et al.* [2012] observed the same decreasing trend from surface flask measurements and found a strong correlation between global average C_2H_6 mixing ratios and CH_4 growth rates from 1985 to 2010, suggesting that these light alkanes have a common source.

There is evidence that the long-term decline in C_2H_6 in the Northern Hemisphere recently reversed [*Franco et al.*, 2015; *Helmig et al.*, 2014a]. The change is postulated to be due to increased emissions tied to the recent growth of shale gas exploration and development in the U.S. [*Franco et al.*, 2016; *Helmig et al.*, 2016]. *Helmig et al.* [2016] estimate a mean C_2H_6 annual emission increase of 0.42 ± 0.19 Tg yr^{-1} between 2009 and 2014 in the Northern Hemisphere, corresponding to an overall 2.1 ± 1.0 Tg yr^{-1} increase of C_2H_6 emissions for the same period. *Franco et al.* [2015] report a sharp increase ($4.90 \pm 0.91\%$ yr^{-1}) in measurements of C_2H_6 columns (molecules cm^{-2}) over the Jungfraujoch site in the Swiss Alps between 2009 and 2014. *Vinciguerra et al.* [2015] also showed a ~25% increase (1.1 ppbv) in hourly mean C_2H_6 surface mixing ratios from 2004 to 2013 at different sites downwind of the Marcellus shale play, one of the largest natural gas producing regions in the U.S. Several recent field measurement campaigns over U.S. natural gas basins have reported very high average mixing ratios of C_2H_6 (up to 300 ± 169 ppbv (1σ) [*Koss et al.*, 2015]), along with other volatile organic compounds (VOCs) [*Gilman et al.*, 2013; *Helmig et al.*, 2014b; *Katzenstein et al.*, 2003; *Pekney et al.*, 2014; *Pétron et al.*, 2012; *Swarthout et al.*, 2013; *Thompson et al.*, 2014], and several studies have found that C_2H_6 is the quantitatively largest nonmethane VOC emitted during oil and natural gas exploitation [*Field et al.*, 2015; *Kort et al.*, 2016; *Vinciguerra et al.*, 2015; *Warneke et al.*, 2014].

Xiao et al. [2008] presented a 2001 global budget for C_2H_6 based on CH_4 emission estimates. They considered the geographical distributions of natural gas production based on production statistics and locations of major oil and gas wells compiled by *Fung et al.* [1991] and compared their results to a suite of observations collected prior to 2004. Therefore, this inventory is expected to be outdated, at least for North America, where the majority of the oil and gas development has occurred since 2004. Although we do not focus on it here, the Hemispheric Transport of Air Pollutants Phase II (HTAP2) is also likely outdated as it requires annual additional 1.2 Tg C_2H_6 emissions from North American sources in 2014 over 2008 emission rates to match C_2H_6 column observations [*Franco et al.*, 2016]. Note that *Franco et al.* [2016] applied that scaling uniformly without focusing on particular geographic regions.

The apparent dynamic nature of C_2H_6 concentrations and the plausible use C_2H_6 as a tracer for CH_4 leakage from the fossil fuel industry serve as motivation for this work. In this study, we present a 2010 C_2H_6 emission inventory (beginning of the increasing trend in the abundance of C_2H_6 reported by *Franco et al.* [2015]) and evaluate the differences between this and a previous 2001 C_2H_6 global emission inventory. To estimate C_2H_6 emissions for the year 2010 outside the U.S., we use a similar approach to *Xiao et al.* [2008], but based on CH_4 emissions derived from 2010 spaceborne CH_4 observations from the Greenhouse Gases Observing SATellite (GOSAT), and we combined this with adjusted C_2H_6 emissions from the most recent bottom-up U.S. National Emission Inventory (NEI 2011). We implement the emission inventories into the Goddard Earth Observing System (GEOS) Chem chemical transport model and compare the C_2H_6 simulation to a global suite of surface air observations, column measurements, and aircraft profiles.

2. Methodology

2.1. GEOS-Chem Model Description and Configuration

We use the 3-D chemical transport model GEOS-Chem version 10-01 with tropospheric chemistry driven by GEOS 5 assimilated meteorological fields, from the Goddard Earth Observing System (GEOS) of the NASA Global Modeling and Assimilation Office [*Bey et al.*, 2001]. This model version includes the Harvard-NASA Emissions Component (HEMCO) version 1.1.005. HEMCO is a stand-alone software component for computing emissions from different sources, regions, and species on a user-defined grid that gives the user the opportunity to combine, overlay, and update a set of data inventories and scale factors [*Keller et al.*, 2014]. Our analysis is based on a $2° \times 2.5°$ resolution simulation for 2010, with an 18 month spin-up. The GEOS-Chem NO_x-O_x-HC-Aer-Br chemistry mechanism includes tropospheric C_2H_6 loss via reaction with OH, Br, and NO_3, with rate constants of $7.66 \times 10^{-12}\exp(-1020/T)$ cm^3 molecule^{-1} s^{-1} [*Sander et al.*, 2011], $2.36 \times 10^{-10}\exp(-6411/T)$ cm^3 molecule^{-1} s^{-1} [*Parrella et al.*, 2012], and 1.4×10^{-18} cm^3 molecule^{-1} s^{-1}, respectively. The reaction rate with NO_3 is slow and is considered unimportant for the lifetime of C_2H_6 [*Atkinson*, 1991; *Atkinson et al.*, 2004; *Calvert et al.*, 2008]. Stratospheric removal of C_2H_6 by Cl is not considered in our simulation, since past studies have estimated it to account for only ~2% of total global loss [*Gupta et al.*, 1998]. The annual mass-weighted mean OH concentration of 8.5×10^5 molecules cm^{-3} in our GEOS-Chem simulation yields a global tropospheric (>100 hPa) annual mean lifetime for C_2H_6 of ~93 days. In the boundary layer (>868 hPa), we

estimated averaged lifetimes of 67 days globally, 41 days over the tropics (23°N–23°S), and 105 days in the middle-to-high latitudes (23°–66°N, 23°–66°S). Based on the analysis in *Naik et al.* [2013] for other models, our global mean OH abundance of 8.5×10^5 molecules cm^{-3} would approximately produce CH_4 and methyl chloroform (CH_3CCl_3) lifetimes of ~11.6 and ~6.7 years, respectively. Both lifetime values are consistent with observation-derived lifetime estimates from *Prinn et al.* [2005] and *Prather et al.* [2012] which range from 10.2 to 11.2 years for CH_4 and 6.0 to 6.3 years for CH_3CCl_3.

The public release version of GEOS-Chem v10-01 (used here) does not include tropospheric halogens other than Br, and this is a source of uncertainty in the following analysis. Although prior studies have shown Cl to be a minor sink for C_2H_6 [*Gupta et al.*, 1998], in a very recent paper, *Sherwen et al.* [2016] conclude that Cl may be an important C_2H_6 sink that can decrease the simulated global burden of C_2H_6 by about ~20%. The lifetime of C_2H_6 is very sensitive to simulated OH, and thus, the interpretation of model-measurement comparisons is always limited by our ability to adequately represent the emissions of other trace gases that compete for reaction with OH.

We use Global Fire Emissions Database Version 3 (GFED3) biomass-burning emissions of C_2H_6 in the simulation by using both anthropogenic C_2H_6 emission inventories [*van der Werf et al.*, 2010]. The GFED3 emission inventory is based on global satellite-derived burned area information from the Moderate Resolution Imaging Spectroradiometer sensor. At a global scale, the estimated uncertainty for biomass burning carbon emissions is around 20% [*van der Werf et al.*, 2010]. GFED3 does not account for many small fires; this may be particularly relevant in the southeastern U.S. during time periods or locations with significant agricultural/prescribed burning [*Randerson et al.*, 2012]. There is interannual variability in the emissions of C_2H_6 from fires globally and over the U.S. (23–50°N, −130 to 60°W). We compared emissions during 11 years (2001–2010) and found that averaged biomass burning C_2H_6 emissions from GFED3 are 2.1 ± 0.35 (1σ) Tg/yr and 0.011 ± 0.0049 (1σ) Tg/yr globally and over the U.S., respectively. During 2001–2011, global C_2H_6 emissions from biomass burning were highest in 2010; however, over the U.S., C_2H_6 emissions were equal to the average emissions for this period.

A detailed description of fossil fuel and biofuel C_2H_6 emissions in our simulations is discussed in section 2.3.3. For emissions of other species such as CO, NO, SO_x, and other VOCs, we use global emission inventories (HTAP2 and Emissions Database for Global Atmospheric Research inventory version 4.2 (EDGAR v4.2)) overwritten by available regional emission inventories for Asia, Canada, Europe, Mexico, and the U.S. The composite of emission inventories corresponds to the public release version of GEOS-Chem v10-01.

We present updated anthropogenic (fossil fuel and biofuel) emissions of C_2H_6 for the year 2010 and compare them to a previous C_2H_6 emission inventory for the year 2001. We also compare the C_2H_6 model simulations based on both emission inventories to a global suite of observations. Our goal is to showcase the differences in anthropogenic emission totals and geographical distributions that are borne out by using different inventories at different points in time. Lastly, we document the impact of C_2H_6 on 2010 simulated atmospheric abundances of O_3 and PAN.

2.2. Global Observations

We compare the model simulations to an exhaustive database of recent C_2H_6 observations at the surface (2010–2011) and airborne campaigns (2008–2014) (Table 1). All observations are summarized in Table 2, and the regions of interest are depicted in Figure 2. We include surface flask measurements made at the Institute of Arctic and Alpine Research (INSTAAR) Global Monitoring Program from samples collected by the National Oceanic and Atmospheric Administration (NOAA) Global Greenhouse Gas Reference Network (GGGRN) (http://instaar.colorado.edu/arl/Global_VOC.html), C_2H_6 column measurements derived from ground-based Fourier transform infrared (FTIR) solar observations from the Network for the Detection of Atmospheric Composition Change (NDACC, http://www.ndsc.ncep.noaa.gov/), and data from recent aircraft campaigns including the Arctic Research of the Composition of the Troposphere from Aircraft and Satellites (ARCTAS) [*Simpson et al.*, 2011; *Simpson et al.*, 2010], the Hiaper Pole-to-Pole (HIPPO) campaign [*Wofsy et al.*, 2012], the Studies of Emissions and Atmospheric Composition, Clouds and Climate Coupling by Regional Surveys (SEAC4RS) [*Blake et al.*, 2014; *Schauffler et al.*, 2014], the 2014 Deriving Information on Surface Conditions from Column and Vertically Resolved Observations Relevant to Air Quality (DISCOVER-AQ) [*Yacovitch and Herndon*, 2014] campaign, and the Front Range Air Pollution and Photochemistry Éxperiment (FRAPPÉ) [*Richter et al.*, 2015]. We also include reported surface measurements from the Boulder Atmospheric Observatory (BAO) [*Gilman et al.*, 2013; *Swarthout et al.*, 2013] and data from 43 Chinese cities [*Barletta et al.*, 2005].

Table 1. C_2H_6 Observations From Surface Sites and Airborne Campaigns Used to Evaluate the Model

2010 Surface Flask Measurements From the NOAA/INSTAAR Global VOC Monitoring Program

Figure 2 Region No.	Mission	Location	Period	Reference
1	ARCTAS	40°–180°W, 32°–90°N	Apr and Jun–Jul 2008	*Simpson et al.* [2010] and *Simpson et al.* [2011]
2	HIPPO	150°E–84°W, 80°N–67°S	Jan and Oct–Nov 2009, Mar–Apr 2010, Jun–Sep 2011	*Wofsy et al.* [2012]
3	SEAC4RS	80°–126°W, 19°–50°N	Aug–Sep 2013	*Blake et al.* [2014] and *Schauffler et al.* [2014]
4	DISCOVER-AQ	103°–105°W, 38°–42°N	Jul–Aug 2014	*Yacovitch and Herndon* [2014]
5	FRAPPÉ	101°–109°W, 38°–42°N	Jul–Aug 2014	*Richter et al.* [2015]

2010 Column Measurements From the NDACC Network

Code	Site	Location	Altitude (masl)	Reference
	North America			
TAO	Toronto, Canada	112°W, 32°N	2158	*Wiacek et al.* [2007]
BLD	Boulder, Colorado, United States	69°W, 77°N	30	*Hannigan et al.* [2009]
Europe				
JFJ	Jungfraujoch, Switzerland	8°E, 47°N	3580	*Franco et al.* [2015]
KRN	Kiruna, Sweden	20°E, 68°N	419	*Blumenstock et al.* [2009] and *Kohlhepp et al.* [2011]
	North Africa			
IZO	Izaña, Tenerife, Spain	16°W, 28°N	2367	*García et al.* [2012] and *Schneider et al.* [2010]

2010 Surface Flask Measurements From the NOAA/INSTAAR Global VOC Monitoring Program

Code	Site	Location	Altitude (masl)
	North America		
ALT	Alert, Nunavut, Canada	62.51°W, 82.45°N	205
BMW	Tudor Hill, Bermuda, United Kingdom	64.88°W, 32.26°N	60
BRW	Barrow, Alaska, United States	156.61°W, 71.32°N	16
CBA	Cold Bay, Alaska, United States	162.72°W, 55.21°N	57
KEY	Key Biscayne, Florida, United States	80.16°W, 25.67°N	6
LEF	Park Falls, Wisconsin, United States	90.27°W, 45.95°N	868
MID	Sand Island, Midway, United States	177.38°W, 28.21°N	15
THD	Trinidad Head, California, United States	124.15°W, 41.05°N	112
UTA	Wendover, Utah, United States	113.72°W, 39.9°N	1332
	Europe		
HPB	Hohenpeissenberg, Germany	11.02°E, 47.8°N	941
ICE	Storhofdi, Vestmannaeyjar, Iceland	20.29°W, 63.4°N	127
MHD	Mace Head, County Galway, Ireland	9.9°W, 53.33°N	26
OXK	Ochsenkopf, Germany	11.81°E, 50.03°N	1172
PAL	Pallas-Sammaltunturi, GAW Station, Finland	24.12°E, 67.97°N	565
SUM	Summit, Greenland	38.42°W, 72.6°N	3215
ZEP	Ny-Alesund, Svalbard, Norway and Sweden	11.89°E, 78.91°N	479
	East Asia		
SHM	Shemya Island, Alaska, United States	174.13°E, 52.71°N	28
TAP	Tae-ahn Peninsula, South Korea	126.13°E, 36.74°N	21
	Central America		
KUM	Cape Kumukahi, Hawaii, United States	154.82°W, 19.52°N	8
MEX	High Altitude Global Climate Observation Center, Mexico	97.31°W, 18.98°N	4469
MLO	Mauna Loa, Hawaii, United States	155.58°W, 19.54°N	3402
	North Africa		
IZO	Izana, Tenerife, Canary Islands, Spain	16.5°W, 28.31°N	2378
ASK	Assekrem, Algeria	5.63°E, 23.26°N	2715
	South Asia		
GMI	Mariana Islands, Guam	144.66°E, 13.39°N	5
	Australia		
BKT	Bukit Kototabang, Indonesia	100.32°E, 0.2°S	850
CGO	Cape Grim, Tasmania, Australia	144.69°E, 40.68°S	164

Table 1. (continued)

2010 Surface Flask Measurements From the NOAA/INSTAAR Global VOC Monitoring Program

Code	Site	Location	Altitude (masl)
	South Africa		
ASC	Ascension Island, United Kingdom	14.4°W, 7.97°S	90
CRZ	Crozet Island, France	51.85°E, 46.43°S	202
HBA	Halley Station, Antarctica, United Kingdom	26.21°W, 75.61°S	35
MKN	Mt. Kenya, Kenya	37.3°E, 0.06°S	3649
SEY	Mahe Island, Seychelles	55.53°E, 4.68°S	6
SYO	Syowa Station, Antarctica, Japan	39.58°E, 69°S	3
SPO	South Pole, Antarctica, United States	24.8°W, 89.98°S	2815
	South America		
EIC	Easter Island, Chile	109.43°W, 27.16°S	69
PSA	Palmer Station, Antarctica, United States	64°W, 64.92°S	15
SMO	Tutuila, American Samoa	170.56°W, 14.25°S	60
TDF	Tierra Del Fuego, Ushuaia, Argentina	68.31°W, 54.85°S	32
	Surface Observations		

| Code/Figure 2 Region No.	Site	Location	Period	Reference
BAO	Boulder Atmospheric Observatory	105.01°W, 40.05°N	Feb–Mar 2011	*Gilman et al.* [2013]
BAO	Boulder Atmospheric Observatory	105.01°W, 40.05°N	Feb–Mar 2011	*Swarthout et al.* [2013]
6	43 Chinese cities averaged horizontally every 20° × 10° (longitude, latitude)	100°–130°E, 20°–45°N	Jan–Feb 2001	*Barletta et al.* [2005]

2.3. Global C_2H_6 Emission Inventories
2.3.1. 2001 C_2H_6 Emission Inventory

Prior to this work, the most recent global C_2H_6 emission inventory implemented in GEOS-Chem model version 10-01 was based on the year 2001 [*Xiao et al.*, 2008]. The model sets this C_2H_6 inventory as default for any simulation. Briefly, this inventory is derived from a previous C_2H_6 emission inventory by *Xiao et al.*

Table 2. C_2H_6 Emissions in Tg yr^{-1} by Region for the 2001 and 2010 C_2H_6 Emission Inventories

Region	Fossil Fuel (Tg yr^{-1})	Biofuel (Tg yr^{-1})	Biomass Burning (Tg yr^{-1})
	2001 C_2H_6 Emission Inventory		
Global	7.9	2.5	2.7
Northern Hemisphere	7.2	2.1	1.1
North America	1.9	<0.05	0.1
Europe	2.1	0.3	<0.05
East Asia	1.6	0.4	0.1
Central America	0.2	0.1	<0.05
North Africa	0.6	0.3	0.4
South Asia	0.8	1.0	0.4
Southern Hemisphere	0.7	0.4	1.7
Australia	0.3	0.1	<0.05
South Africa	0.2	0.2	0.7
South America	0.1	0.2	1.0
	2010 C_2H_6 emission Inventory		
Global	7.1	2.8	2.7
Northern Hemisphere	6.7	2.4	1.1
North America	1.7	<0.05	0.1
Europe	1.6	0.4	<0.05
East Asia	1.9	0.4	0.1
Central America	0.4	0.1	<0.05
North Africa	0.4	0.4	0.4
South Asia	0.8	1.0	0.4
Southern Hemisphere	0.4	0.4	1.7
Australia	0.1	0.1	<0.05
South Africa	0.1	0.3	0.7
South America	0.2	0.1	1.0
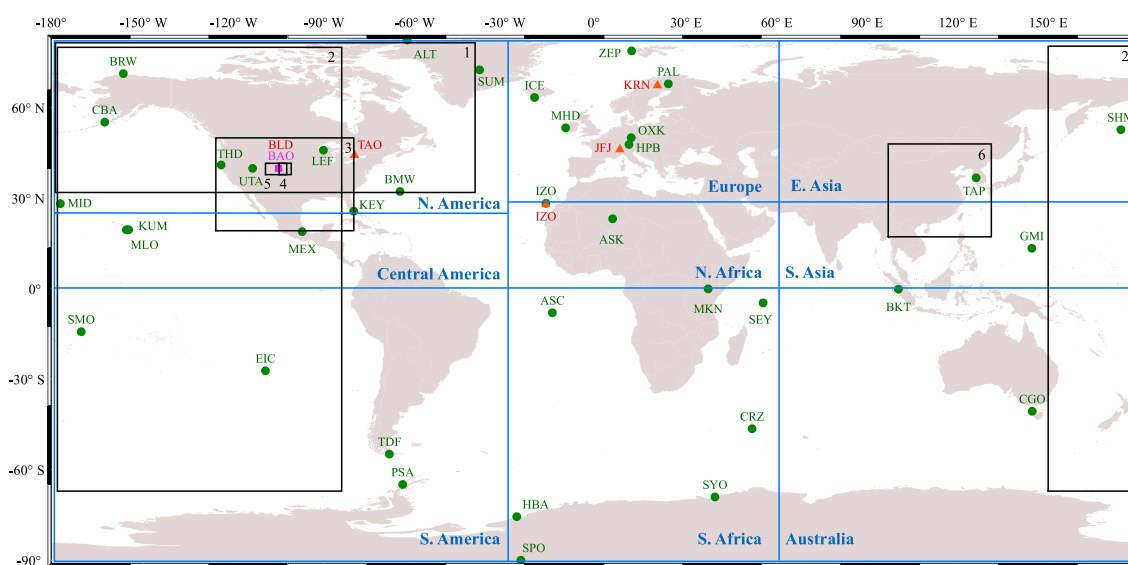
Figure 2. Regions for C_2H_6 emissions analysis and locations of C_2H_6 observations. The black boxes cover regions of aircraft measurements, the green circles represent surface flask measurements, the orange triangles locate C_2H_6 column measurements, and the purple square shows BAO surface measurements (Table 1). Regions delimited to calculate C_2H_6 emissions presented on Table 2 are encompassed by blue boxes.

[2004], which scales C_2H_6 emissions to CH_4 fossil fuel sources by using fixed regional ratios, and bases the geographical distribution for the emissions on data from 1978 to 1986 [*Fung et al.*, 1991; *Wang et al.*, 2004]. Major changes to the distribution of fossil fuel sources may have occurred globally during the period from which they draw data for the model evaluation. *Xiao et al.* [2008] estimate global C_2H_6 emissions for three different source types: (1) fossil fuel, (2) biofuel (domestic wood fuels), and (3) biomass burning. However, the only global C_2H_6 emission inventory from *Xiao et al.* [2008] implemented in GEOS-Chem version 10-01 is from fossil fuel sources. In the model, the C_2H_6 emission fluxes from the fossil fuel inventory from *Xiao et al.* [2008] have no seasonality, and no scaling factors are available to scale them to other years. To simulate global biofuel sources, we use the biofuel C_2H_6 emission inventory derived by *Yevich and Logan* [2003] and the GEFD3 emission inventory [*van der Werf et al.*, 2010] for biomass burning C_2H_6 emissions.

2.3.2. 2010 C_2H_6 Emission Inventory
2.3.2.1. Global C_2H_6 Emissions

We develop an updated global C_2H_6 emission inventory for 2010, by scaling C_2H_6 to CH_4 emissions following a similar approach to previous studies [*Blake and Rowland*, 1986; *Etiope and Ciccioli*, 2009; *Franco et al.*, 2016; *Rudolph*, 1995; *Xiao et al.*, 2004; *Xiao et al.*, 2008]. There are many approaches that can be used to estimate CH_4 emissions (i.e., top-down studies, bottom-up models, inventories, and data-driven approaches), and differing approaches can yield different emission totals, attribution, or geographical distributions [*Saunois et al.*, 2016]. In this study, the CH_4 fluxes were derived from the Greenhouse Gases Observing SATellite (GOSAT) by *Turner et al.* [2015] for the year 2010. To derive anthropogenic CH_4 emissions, *Turner et al.* [2015] used a priori emissions from EDGAR v4.2 (http://edgar.jrc.ec.europa.eu/). The EDGAR emission inventory combines Tier 1 and region-specific Tier 2 emission factors, which have multiple uncertainties associated with them. A detailed description of these uncertainties is presented by *Olivier* [2002]. The estimated uncertainty of satellite CH_4 single retrievals is 0.8% [*Parker et al.*, 2011]. A description of the error characterization and the uncertainties associated with the North American CH_4 inversions can be found in *Turner and Jacob* [2015]. *Turner et al.* [2015] infer a 2009–2011 U.S. anthropogenic emission source of 40.2–42.7 Tg a^{-1} and attribute 22–31% to oil and gas activities. Other inverse studies have inferred a larger range of anthropogenic emissions (30.0–44.5 Tg a^{-1}) [see *Turner et al.*, 2015, and references within]. It is important to note that, over regions with CH_4 emissions from oil and natural gas activities and livestock, the source attribution is very sensitive to assumptions made in the prior distribution. Uncertainties associated with the CH_4 emissions, or their attribution, are only one of several sources of uncertainty in using CH_4 fluxes to estimate C_2H_6 fluxes. As we discuss later in this section, a second major issue is the choice of C_2H_6/CH_4 emission ratio.

We implement two grid resolutions for the *Turner et al.* [2015] CH_4 fluxes for the year 2010. For North America, we use CH_4 emission fluxes at $1/2° \times 2/3°$ resolution and at $4° \times 5°$ resolution for the rest of the world. Considering the uncertainties in the attribution of fluxes, we expect a better agreement of CH_4 anthropogenic sources at a coarse resolution compared to the finer resolution. We can have the most confidence in the total fluxes, rather than fine sectorial attribution. From the 12 anthropogenic CH_4 source categories derived in *Turner et al.* [2015], 3 are relevant to C_2H_6: natural gas activity, biofuel usage, and biomass burning.

We consider natural gas activity and biofuel source categories and retain the GFED3 emission inventory for emissions of C_2H_6 from biomass burning during 2010. We treated biofuel consumption (both from home cooking and heating) as residential biomass burning and thus applied a temperate forest fuel ratio of 15.2 (% mol C_2H_6/mol CH_4), as estimated by *Akagi et al.* [2011]. To derive C_2H_6 emissions from CH_4 fluxes associated with natural gas activity, we used a ratio of 4.3 (% mol C_2H_6/mol CH_4) based on mixing ratio enhancements estimated from the South Central U.S. by *Katzenstein et al.* [2003]. *Warneke et al.* [2014] observed similar emission ratios during wintertime 2012 over the Uintah Basin. In this study, we assume that the observed enhancement ratios (slopes of the linear fits) are approximately equivalent to the emission ratios since C_2H_6 is a relatively long-lived species and in situ measurements are taken close to the sources.

2.3.2.2. Constraints on C_2H_6 Emissions Over Mexico and Asia

An analysis of the resulting global C_2H_6 emissions immediately points to likely problems with the underlying CH_4 fluxes or the 4.3 (% mol C_2H_6/mol CH_4) ratio over Mexico and Asia. Also, estimated fossil fuel C_2H_6 emission totals derived from CH_4 fluxes over Mexico are 2 times higher (0.23 Tg) than the 2001 C_2H_6 emission inventory. Similar differences of 0.36 Tg and 0.13 Tg occur when comparing to RETRO (REanalysis of the TROpospheric chemical composition 2000, http://gcmd.gsfc.nasa.gov/records/GCMD_GEIA_RETRO.html) and Global Emissions InitiAtive 1985 (http://www.geiacenter.org) emission inventories, respectively. Additionally, when analyzing the spatial distribution of fossil fuel C_2H_6 emissions over Mexico derived from CH_4 fluxes, we find that the C_2H_6 emission sources are located away from oil and natural gas production areas. Second, total fossil fuel satellite-derived emissions of C_2H_6 over Asia are half (~1.2 Tg) of the 2001 C_2H_6 emission inventory and RETRO, respectively. A simulation with these emissions produces C_2H_6 mixing ratios that are 1/6 of the observed mixing ratios during wintertime in 2001 by *Barletta et al.* [2005] (note also the time difference between these in situ observations (2001) and the inversion (2010)). Finally, a comparison between the spatial distribution of fossil fuel C_2H_6 emissions over China from the 2010 C_2H_6 emission inventory and the emissions derived from CH_4 fluxes shows that the C_2H_6 emissions from CH_4 fluxes are clustered in south central China, while the *Xiao et al.* [2008] C_2H_6 emission distribution covers urban and known oil and natural gas-producing regions in China. In summary, there is evidence that scaling C_2H_6 emissions derived from CH_4 fluxes does not produce realistic C_2H_6 emission over Mexico and China. In order to address the two regional discrepancies above, we substitute the C_2H_6 emissions derived from CH_4 fluxes with the *Xiao et al.* [2008] C_2H_6 emission inventory over Mexico and Asia (including China, India, Indonesia, Japan, Mongolia, and North and South Korea).

2.3.2.3. Constraints on C_2H_6 Emissions Over the U.S.

The NEI 2011 emission data are provided by state and local agencies based on industrial, commercial, and area sources. We incorporate NEI 2011 version 2 C_2H_6 emissions on a $0.1° \times 0.1°$ grid for biofuel and six anthropogenic source categories, including oil and gas activities [*U.S. Environmental Protection Agency*, 2013]. GEOS-Chem version 10-01 uses a scaling factor of 1.016 to apply NEI 2011 C_2H_6 emissions to the year 2010. For other species such as CO, NO, and other VOCs, scaling factors are assigned based on government statistics and documents. For industrial emissions, the scaling factors are based on reported trends from the Environmental Protection Agency Acid Rain Program (https://www.epa.gov/airmarkets/acid-rain-program). For other emissions the scaling factors come from the National Emissions Inventory Air Pollutant Emissions Trends data (https://www.epa.gov/air-emissions-inventories/air-pollutant-emissions-trends-data).

The NEI 2011 C_2H_6 emission sources appear to align with the distribution of active oil and natural wells over the U.S. (see Figure 5); however, when the GEOS-Chem-simulated C_2H_6 is compared to aircraft measurements over the U.S. from five recent field campaigns (2008–2014) and 2010 surface flask observations from the NOAA GGGRN, the use of the NEI 2011 emissions produces mixing ratios at the surface and throughout the column that are 14–50% of those observed. Consequently, we tested uniformly scaling C_2H_6 emissions from all the categories in the NEI 2011 by factors between 1.2 and 2, and we compared the results to the

Figure 3. Spatial distribution of averaged percentage molar C_2H_6/CH_4 ratios in oil and natural gas basins over the contiguous U.S. The values and sizes of the circles represent the magnitude of the ratios in each basin. South Central U.S.: calculated using annual emissions of C_2H_6 and CH_4 reported by *Katzenstein et al.* [2003]. Bakken: *Brandt et al.* [2015] as reported by *Kort et al.* [2016]. Barnett: *Speight* [2013] as reported by *Kort et al.* [2016]. Denver-Julesburg: *Peischl et al.* [2015a]. Eagle Ford: *Conder and Lawlor* [2014] and *Ghandi et al.* [2015] as reported by *Kort et al.* [2016]. Fayetteville: average from *Peischl et al.* [2015b] and *Speight* [2013] as reported by *Kort et al.* [2016]. Green River: *Peischl et al.* [2015a]. Haynesville: average from *Peischl et al.* [2015b] and *Speight* [2013] as reported by *Kort et al.* [2016]. Marcellus: average from *Peischl et al.* [2015b], 2009 U.S. Geological Survey (USGS) database as reported by *Peischl et al.* [2015b], and *Conder and Lawlor* [2014] as reported by *Kort et al.* [2016]. Permian: *Peischl et al.* [2015a]. Western Arkoma: average from *Peischl et al.* [2015b], 2009 U.S. Geological Survey (USGS) database as reported by *Peischl et al.* [2015b]. Uintah: average from *Helmig et al.* [2014b] and *Warneke et al.* [2014]. Utica: *Conder and Lawlor* [2014] and *Ghandi et al.* [2015] as reported by *Kort et al.* [2016].

observations. For all factors, a linear regression of 2010 monthly mean surface flask observations over the U.S. versus model output yields coefficient of determination (R^2) values between 0.59 and 0.64. The slopes range from 0.8 to 1.0. Of the scaling factors tested, 1.4 produces the best agreement between the GEOS-Chem simulation and observations in regions *without* major oil and gas operations. Therefore, we multiplied NEI 2011 C_2H_6 emissions by 1.4, which represents an addition of 0.5 Tg of C_2H_6 compared to the base NEI 2011. Scaling beyond 1.4 results in an overestimate of observations in these regions. Following the adjustment of NEI 2011 C_2H_6 emissions, we refer to the resulting global C_2H_6 emission inventory as *2010 C_2H_6 emission inventory*. Thus, the 2010 C_2H_6 emission inventory combines a global C_2H_6 emission inventory derived from satellite CH_4 observations, except for Mexico and Asia where we apply previous emission estimates, and a regional C_2H_6 emission inventory derived by adjusting NEI 2011 C_2H_6 emissions.

2.3.2.4. Uncertainties

Although the approach of deriving C_2H_6 from CH_4 emissions is consistent with past global budget studies, large uncertainties are associated with the use of few C_2H_6/CH_4 emission ratios, especially for the natural gas industry, which in the last decade has been subject to multiple emission controls in many countries. Emission ratios depend on the type of oil and natural gas reservoir (e.g., tight gas versus shale gas), the VOC composition of the natural gas [*Warneke et al.*, 2014], the production stage of a producing well [*Kang et al.*, 2014; *Pacsi et al.*, 2015], among other characteristics. There has been significant attention devoted to documenting C_2H_6 to CH_4 enhancement ratios. Given the lifetime of each species, enhancement ratios observed near defined sources are often a reasonable surrogate for emission ratios. Figure 3 presents a summary of averaged percentage molar C_2H_6/CH_4 ratios observed in different oil and natural gas basins over the contiguous U.S. The reported ratios (% mol C_2H_6/mol CH_4) have a large range; for example, *Kort et al.* [2016] report 40.5 for the Bakken, more than an order of magnitude larger than the ratio reported for some oil and gas basins in the central U.S. [*Peischl et al.*, 2015b]. There are a number of problems associated with basing C_2H_6 emissions on CH_4 emissions and dynamic C_2H_6/CH_4 emission ratios. As we will show later, using a constant C_2H_6/CH_4 emission ratio over regions with high emission gradients (e.g., U.S.) does not represent the geographical distributions of the emissions and the resulting atmospheric abundances of C_2H_6. Section 4.1 presents the sensitivity of our findings to the choice of C_2H_6-to-CH_4 molar ratios through simulations with a fixed ratio applied broadly across the U.S. by using the low and high ratios available from the recently published literature (Figure 3).
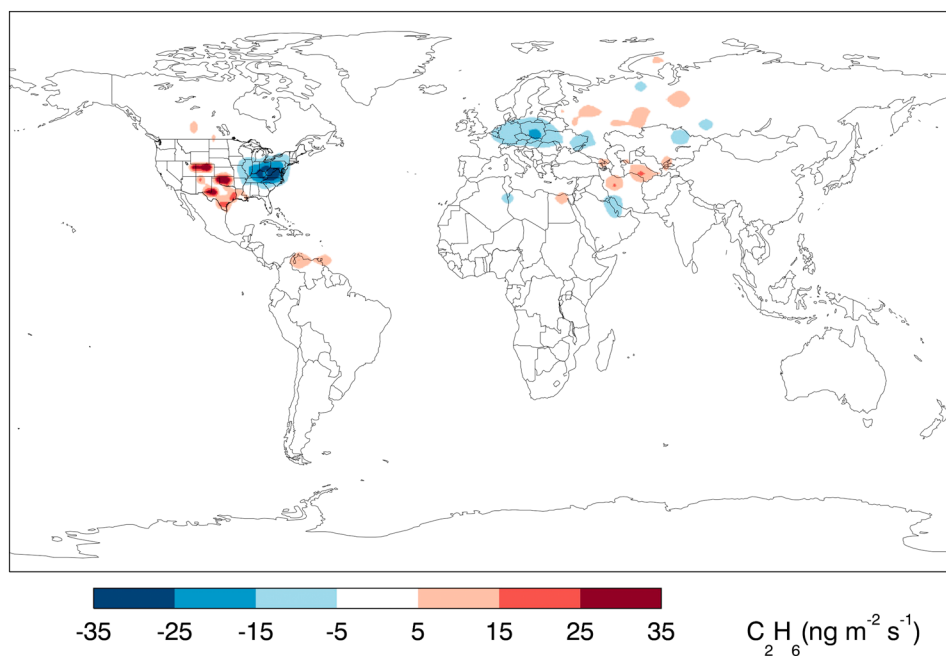
Figure 4. Global comparison between modeled distributions of fossil fuel C_2H_6 emissions for 2001 and 2010 C_2H_6 emission inventories (2010–2001). The positive values (warmer colors) represent increases in modeled annual mean C_2H_6 emission fluxes.

2.3.3. Comparison Between the 2001 and 2010 C_2H_6 Emission Inventories

Table 2 shows global and regional C_2H_6 emission estimates for both emission inventories. For the 2010 C_2H_6 emission inventory, Northern Hemisphere fossil fuel sources represent half of global C_2H_6 emissions and 95% of global fossil fuel emissions.
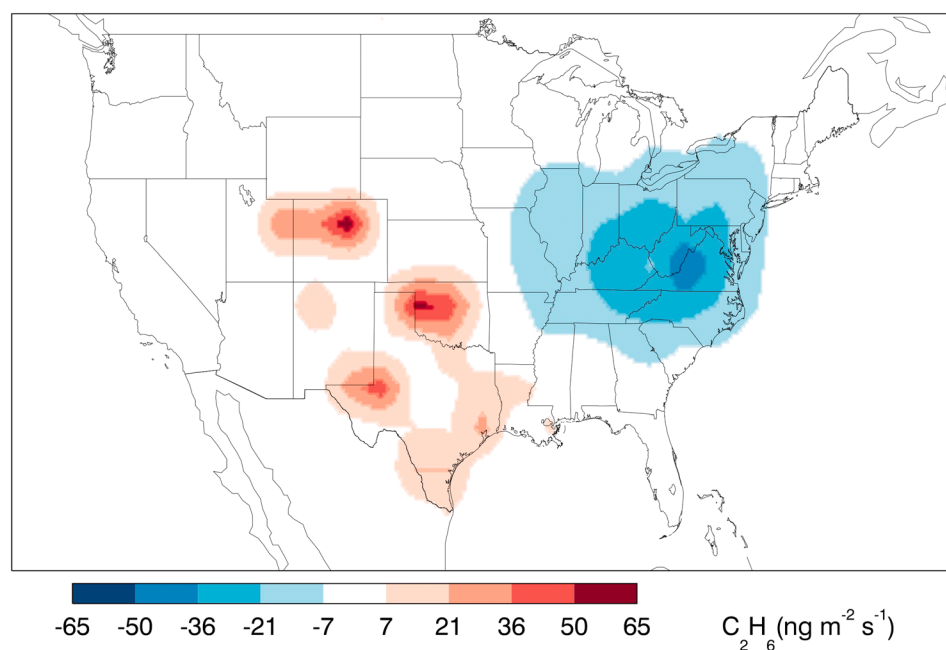
Figure 5. Comparison between modeled distributions of fossil fuel C_2H_6 emissions for 2001 and 2010 C_2H_6 emission inventories (2010–2001) over the U.S. The positive values (warmer colors) represent increases in modeled annual mean C_2H_6 emission fluxes.
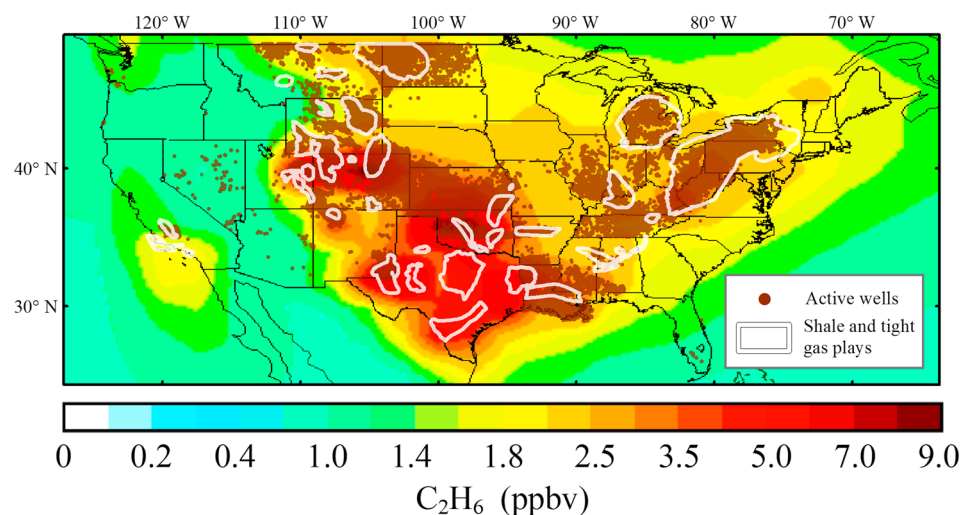
Figure 6. Modeled annual mean surface mixing ratios of the 2010 C_2H_6 emission inventory and spatial distribution of active wells (FracTracker, accessed Nov 2015, www.fractracker.org; data for Maryland, North Carolina, and Texas are missing). Shale and tight gas plays (Energy Information Administration, accessed Dec 2014, www.eia.gov/dnav/ng/ng_sum_lsum_a_EPG0_xdg_count_a.htm) are shown to provide a sense for well distribution over states where well location data are missing.

The C_2H_6 emission totals are only subtly different between both global inventories; however, the spatial distributions of the emissions are quite distinct. In our recommended 2010 inventory, C_2H_6 emissions increase over intense oil and gas-producing regions, including the central and northeastern U.S., Venezuela, eastern Russia, and the northern part of the Middle East (Figure 4). We point this out because it may indicate that emissions from the oil and natural gas industry in these regions could be important but may not be accounted for in commonly used inventories. Over Europe, *Xiao et al.* [2008] concluded that their inventory overestimated the observed C_2H_6 mixing ratios by 20–30%, and they attributed this in part to an overestimation of European sources. Our 2010 C_2H_6 emission inventory shows a similar reduction of C_2H_6 European sources (Table 2). Over the contiguous U.S., we find important differences in the geographical distribution and magnitude when comparing the fossil fuel C_2H_6 emission fluxes from the 2010 C_2H_6 emission inventory to the *Xiao et al.* [2008] 2001 emission inventory (Figure 5). Fossil fuel C_2H_6 emission fluxes are smaller over the northeastern part and larger over the central and south central parts of the U.S.

The 2010 C_2H_6 emission inventory shows increased emission regions encompassing major U.S. natural gas production basins (Figure 6). The simulated surface C_2H_6 abundances produced by the 2010 C_2H_6 emission inventory closely align with oil and gas activities over the U.S. Although the 2010 C_2H_6 emissions show significant increases in fossil fuel C_2H_6 emissions over these regions, they continue to underestimate the most recent vertical and surface observations of C_2H_6 mixing ratios over the central U.S., as described in section 4. Despite the underestimation of C_2H_6 abundances over the central U.S., the 2010 C_2H_6 emission inventory produces a better geographical distribution of fossil fuel C_2H_6 sources over North American regions and elsewhere compared to the 2001 C_2H_6 emission inventory.

3. Model Evaluation

3.1. Ground-Based C_2H_6 Column Observations

Comparisons between each modeled emission inventory and monthly mean C_2H_6 total columns at selected NDACC stations over the Northern Hemisphere for both C_2H_6 emission inventories are shown in Figure 7. We note that observations over Northern Hemisphere continental regions such as Asia and the Middle East are needed to evaluate model outputs in other oil and natural gas-producing regions.

Ethane columns are derived from ground-based FTIR solar observations following the methodology presented by *Franco et al.* [2015]. The information content as well as the vertical sensitivity for the FTIR retrievals from all the sites we analyze in this paper is similar to the one presented in *Franco et al.* [2015]. At
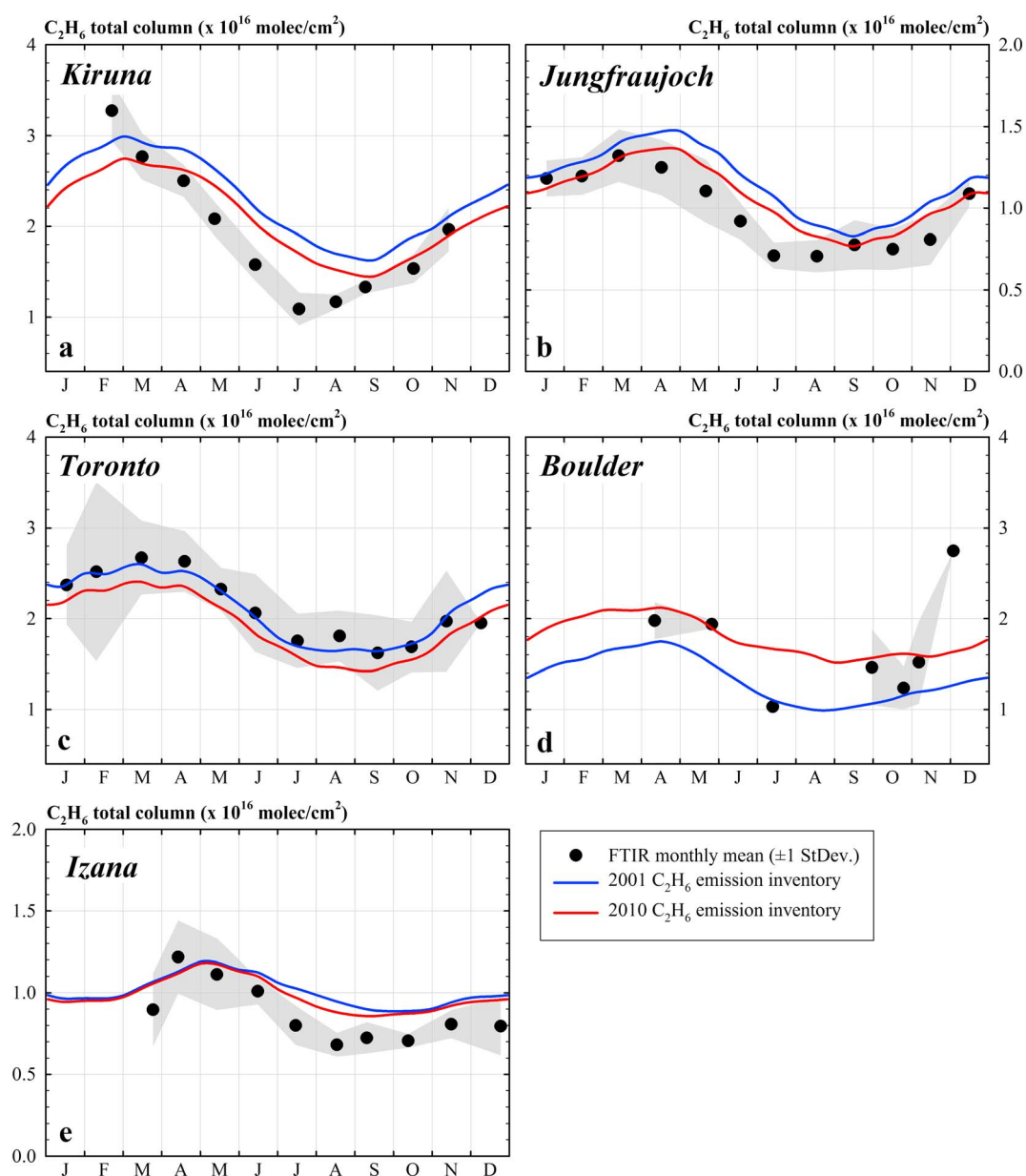
Figure 7. Comparison of 2010 C_2H_6 total columns to modeled 2001 and 2010 C_2H_6 emission inventories. The black dots represent monthly mean C_2H_6 total columns, and the grey areas denote their associated 1σ standard deviation. The lines represent modeled total columns for different emission inventories.

altitudes below 13 km, 99% of the information content is independent from the a priori profile, indicating a very good sensitivity to the true state of the atmosphere [*Franco et al.*, 2015].

The FTIR total column observations largely reflect the tropospheric background, and not solely the surface C_2H_6 abundances. Thus, similarities between our two simulations can be expected, particularly since most FTIR stations involved here are not located in source regions and C_2H_6 has a relative long lifetime that allows emissions to impact abundances at a hemispheric scale. Our model simulations largely reproduce C_2H_6 column observations at the selected stations, suggesting that the OH losses and emissions of other OH-reactive species are being well represented. Additionally, the spatial variability indicates that the model reproduces the major features of C_2H_6 emissions and the most important transport processes. The agreement with observations is particularly good at Toronto and Boulder (see Figure 10; explained on section 4.2). However, during summertime, GEOS-Chem overestimates the C_2H_6 column at three sites (Izana, Kiruna, and Jungfraujoch;
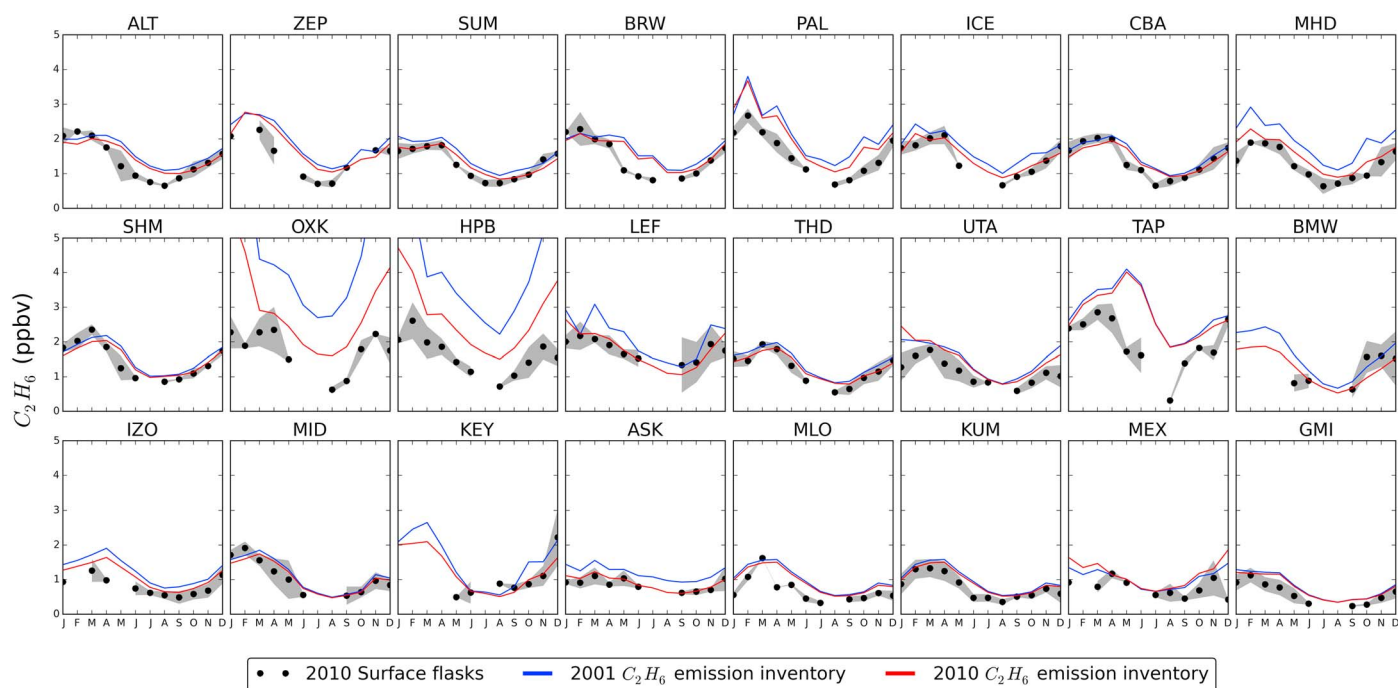
Figure 8. Comparison of Northern Hemisphere 2010 C_2H_6 surface mixing ratios to modeled 2001 and 2010 C_2H_6 emission inventories. The black dots represent C_2H_6 observations from NOAA GGGRN global surface flask network, and the grey areas denote their associated 1σ standard deviation. The lines represent model mixing ratios at the surface from both C_2H_6 emission inventories. The stations are ordered from higher to lower latitudes.

Figures 7a, 7b, and 7e). A similar bias was also reported by *Franco et al.* [2016] over remote sites in the Arctic and the Tropics. The same version of the GEOS-Chem model we use here was also used in that study, and the summertime bias may be driven by ~10–15% lower global mean OH in GEOS-Chem version 10-01 compared to previous versions. *Xiao et al.* [2008] used GEOS-Chem version 6.01.03, and their results do not show a summertime bias compared to surface data. GEOS-Chem version 6.01.03 had a 15% greater C_2H_6-OH rate constant ($8.7 \times 10^{-12}\exp(-1020/T)$ cm^3 molecule^{-1} s^{-1} [*Sander et al.*, 2003]) and ~3% lower annual mean OH concentration (10.2×10^5 molecules cm^{-3}) compared to GEOS-Chem version 10-01 used in this study.

3.2. Surface Observations

Figure 8 presents a comparison between 2010 Northern Hemisphere C_2H_6 surface mixing ratios and the 2001 and 2010 C_2H_6 emission inventories. The Southern Hemisphere comparison is presented in Figure S1 in the supporting information. In both figures, sampling stations are ordered from higher to lower latitudes. The NOAA sampling stations are mostly located at remote locations around the globe, largely avoiding the impact of local anthropogenic emissions.

Mixing ratios at the surface reflect the C_2H_6 latitudinal gradient with values decreasing with decreasing latitude. Our model simulations largely capture the C_2H_6 seasonal cycles. However, the model overestimates surface mixing ratios over Europe (Ochsenkopf (OXK) and Hohenpeissenberg (HPB) stations) by ~160% and ~80% on average for the 2001 and 2010 C_2H_6 emission inventories, respectively. The difference between the model outputs and the observations might be due to an overestimation of European sources. The overestimation we find when simulating 2010 C_2H_6 emissions may be related to incorrect source attribution of European C_2H_6 anthropogenic sources derived from the EDGAR v4.2 inventory used as a prior for the satellite-derived CH_4 fluxes. In Asia, the model overpredicts the C_2H_6 abundance at the Tae-ahn Peninsula (TAP) station located in the southern part of South Korea by ~1 ppbv throughout the year. TAP is likely heavily influenced by emissions from both Russia and China. However, a comparison with surface measurements in 43 Chinese cities [*Barletta et al.*, 2005] shows that the model underpredicts surface mixing ratios for the 2001 wintertime by up to a factor of 3. Given the limited and outdated observations in this region, we cannot determine whether this is a result of
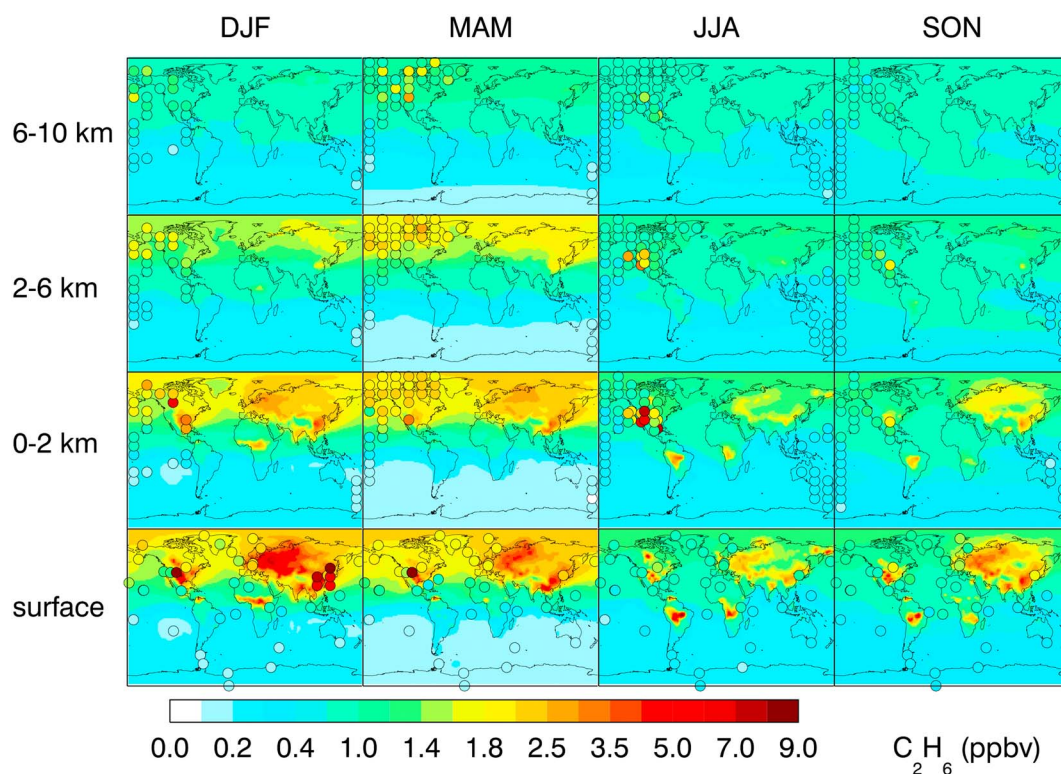
Figure 9. Global mean distribution of C_2H_6 for different seasons and altitude ranges compared to observations from Table 1. The background solid contours are model outputs for 2010 C_2H_6 emissions. The filled circles represent seasonal averages from observations. Aircraft measurements (0–2, 2–6, and 6–10 km) are averaged vertically for each altitude range and horizontally every $20° \times 10°$ (longitude, latitude). Wintertime surface measurements over 43 Chinese cities are averaged horizontally every $20° \times 10°$ (longitude, latitude). The overlapping circles represent averaged results from various observations.

incorrect emissions or an incorrect distribution of emissions. Compared to the rest of the observations we show, there is also a large temporal mismatch between the simulation year (2010) and the Chinese observations (2001). Although our analysis focuses on the Northern Hemisphere, we note that, over the Southern Hemisphere, the station Cape Grim (CGO), located in Tasmania, Australia, is the only station (Figure S1) with large differences between simulations and observations. Specifically, 2001 C_2H_6 emissions produce mixing ratios at the surface almost twice as large as those observed. This difference can be attributed to lower C_2H_6 emissions derived from CH_4 satellite observations compared to the 2001 C_2H_6 emission inventory.

3.3. Vertical Distribution

A comparison between the observed global distribution of C_2H_6 and the GEOS-Chem model output for 2010 C_2H_6 emissions from the surface to 10 km is presented in Figure 9. The background solid contours are the model output from 2010, and the filled circles represent the seasonal averages from the observations compiled in Table 2. Measurements at the surface (lower panel) correspond to seasonal averages from the 2010 surface flask-sampling sites and two measurements taken at the Boulder Atmospheric Observatory (BAO) in Colorado, U.S., during February and March of 2011 [*Gilman et al.*, 2013; *Swarthout et al.*, 2013]. The aircraft observations are plotted as the averages for each altitude range for individual $20° \times 10°$ grid boxes. We plot the data this way, instead of averaged vertical profiles for individual regions/campaigns, because the observations show large gradients over relatively small areas. We compare the model output from 2010 to the aircraft observations collected over the period of 2008–2014. Since the aircraft data represent a relatively short snapshot of time (15–59 flights over 3–20 weeks), this represents a source of uncertainty in the model evaluation as the model output represents seasonal averages.

Surface measurements are generally well simulated by the model throughout the year. However, during the winter, the model tends to overpredict the surface mixing ratios over Europe. The vertical distribution of

C_2H_6 mixing ratios over the U.S. will be discussed in the next section. A comparison between Northern Hemisphere observations and modeled mixing ratios outside the U.S. (not shown) reveals that springtime C_2H_6 mixing ratios from HIPPO over latitudes $<\sim35°$ are the most underpredicted observations (up to 1.5 ppbv). Springtime HIPPO measurements were taken during the same year of the model simulation and the 2010 C_2H_6 emission inventory. The missing C_2H_6 source might be due to an underestimation of biomass burning over the tropics and subtropics or potentially point to remaining issues with East Asian emission inventories.

4. Model-Data Comparison Over the Contiguous U.S.

4.1. Model Comparison to Aircraft Campaigns and Surface Observations

Multiple recent field campaigns, as well as surface observations over the contiguous U.S., allow us to deepen our analysis of anthropogenic C_2H_6 sources and their regional effects on atmospheric mixing ratios. Figure 10 presents a comparison between the observed distribution of C_2H_6 and the GEOS-Chem model output for 2010 C_2H_6 emissions over the U.S. At the surface (lower panel), we show seasonal averages from five surface flask-sampling stations and two sets of measurements collected at the Boulder Atmospheric Observatory during February and March of 2011 [*Gilman et al.*, 2013; *Swarthout et al.*, 2013]. In this figure, aircraft measurements (0–10 km above the ground) were averaged vertically for each altitude range and horizontally every $5° \times 5°$.

In the upper troposphere (upper panel; 6–10 km) the model agrees with the observations except for the central U.S. Here the model overestimates the summertime observed mixing ratios by up to a factor of ~3 (0.5 ppbv). Below 6 km, the model is consistently lower than the observations over the central and southeast U.S. Despite scaling up the NEI 2011 emissions, the model continues to underpredict by a factor of ~4 the observed abundances of C_2H_6 in the central states of Colorado, Wyoming, Nebraska, and Kansas where there is substantial natural gas and oil extraction (Figure 6). The model resolution of $2° \times 2.5°$ can explain some of the discrepancies between the observations and the model output. Also, we note that the data presented in Figure 10 are primarily from aircraft campaigns and the uncertainties (as discussed in section 2.3.2) associated to the temporal mismatch between the aircraft data (2008–2014) and the model (2010) can potentially be greater due to the increase of oil and natural gas extraction over the U.S. during this period [*U.S. Environmental Protection Agency*, 2015]. There are greater discrepancies between the most recent field campaigns (SEAC4RS [*Blake et al.*, 2014; *Schauffler et al.*, 2014], DISCOVER-AQ [*Yacovitch and Herndon*, 2014], and FRAPPÉ [*Richter et al.*, 2015]) and the 2010 model outputs. In order to explore this issue, we used the observed 5% yr^{-1} annual rate of change of C_2H_6 total column over the 2009–2014 time period at midlatitudes reported by *Franco et al.* [2016] to scale the observations to the year 2010. Unfortunately, underpredictions of mixing ratios across the entire column persist, suggesting that the annual rates of change over these intense oil and natural gas regions are greater than 5% yr^{-1} (as reported at the Boulder FTIR station [*Franco et al.*, 2016]). We cannot rule out the influence of smoke plumes on aircraft measurements during SEAC4RS, since 6 out of 26 flights intercepted smoke plumes. However, the FRAPPÉ flights did not intercept major biomass burning plumes, suggesting that neither agricultural burning nor wildfire smoke is responsible for the observed discrepancy, at least during summer 2014. The wide spatial coverage of the underprediction suggests a regional impact of oil and natural gas emissions to C_2H_6 mixing ratios.
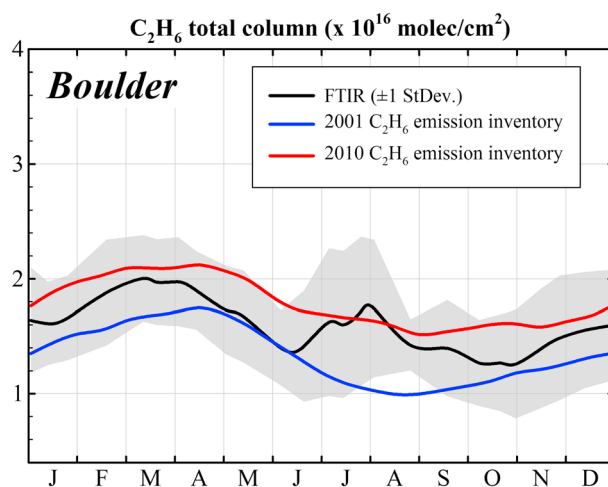
To investigate the impact of considering the most extreme measured molar C_2H_6/CH_4 ratio observed over oil and natural gas regions, we did an additional simulation to derive global C_2H_6 emissions from CH_4 fluxes of fossil fuels, but using a value of 40.5 (percentage of mol C_2H_6/mol CH_4) [*Kort et al.*, 2016]. This extreme choice results in C_2H_6 emissions that are ~7 times greater than the NEI 2011 oil and gas source category. Even though the higher molar ratio (40.5 percentage of mol C_2H_6/mol CH_4) is based on observations taken over the Bakken basin, the use of this ratio produces atmospheric C_2H_6 distributions consistent with aircraft observations over the U.S. central region up to 6 km above the ground. The similar values are consistent with the strong underestimation of the underlying NEI 2011 C_2H_6 emissions over the Central U.S. It is not appropriate to apply the Bakken molar ratio broadly, but the improvement in representing observed mixing ratios over intense oil and natural gas regions suggests that where sufficient information is available, the use of regional emission ratios instead of a fixed nationwide value for all anthropogenic sources may better reproduce C_2H_6 atmospheric abundances. Emission impacts from basins/regions with rapid increase oil and natural gas
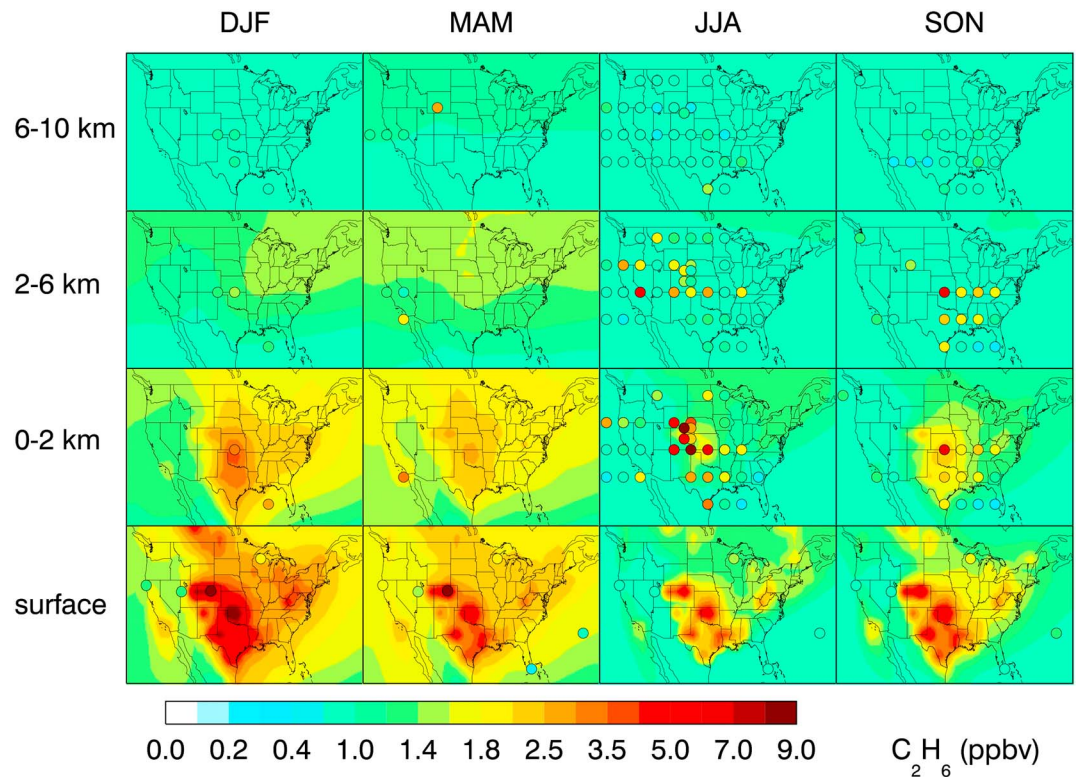
Figure 10. Mean mixing ratios of 2010 C_2H_6 emissions over the U.S. for different seasons and altitude ranges compared to observations from Table 1. The background solid contours are model outputs. The filled circles represent seasonal averages from observations. Aircraft measurements (0–2, 2–6, and 6–10 km) were averaged vertically for each range of altitude and horizontally every 5° × 5° (longitude, latitude). The overlapping circles represent averaged results from various observations.

production like the Bakken shale [*Kort et al.*, 2016] could be better represented by using local emission estimates, which account for the type of oil and natural gas reservoir and the local VOC composition of the natural gas. Our simulations do not show significant emissions from the Bakken shale since the rapid production increase of this basin began in the year 2010 (same year of our simulation [*Peischl et al.*, 2016]).

4.2. Boulder C_2H_6 Column Observations

Over the U.S., we present the results of the 2010 C_2H_6 column measurements from the National Center for Atmospheric Research Boulder station in Figure 7. The Boulder station is located in a region with intensive oil and natural gas production [*Gilman et al.*, 2013; *Pétron et al.*, 2012; *Pétron et al.*, 2014; *Swarthout et al.*, 2013; *Thompson et al.*, 2014]. Unfortunately, there are limited data available for 2010; therefore, we present in Figure 11 a comparison between the model output and the C_2H_6 total column observations by using detrended and scaled data for the period of 2010–

Figure 11. Comparison of C_2H_6 total column to 2010 model output at the Boulder site. The black line represents measurements of C_2H_6 total columns over the period of 2010–2014 detrended and scaled to the year 2010 and the grey areas their associated 1σ standard deviation. The blue and red lines represent modeled total columns for different emission scenarios. We note that 2012 was a high wildfire year for the Rocky Mountain region.

2014 onto the year 2010 by using the same methodology and according to the annual rates of change reported by *Franco et al.* [2016]. This removes the effect of the observed C_2H_6 decrease prior to 2009 and its increase from 2009 onward [*Franco et al.*, 2016]. For the Boulder site, the C_2H_6 total column and GEOS-Chem model output comparison accounts for the altitude difference between the Boulder station and the coarse model grid cell, as explained in *Franco et al.* [2016]. The individual mixing ratio profiles from GEOS-Chem were regridded onto the vertical FTIR layer schemes by using a mass-conservative interpolation that preserves the total C_2H_6 mass above the station altitude and ignores the mass underneath.

The model outputs for both C_2H_6 emission inventories encompass the observed C_2H_6 total columns. Compared to the 2001 C_2H_6 emission inventory, the C_2H_6 total columns produced by the 2010 inventory stay almost all year round within a one standard deviation from the observations. Also, the 2010 C_2H_6 emission inventory produces a seasonality with broader maximum and minimum features that are in line with the observations.

5. Global Contribution of Fossil Fuel C_2H_6 Emissions to O_3 and PAN Mixing Ratios

Ethane is a precursor for both O_3 and PAN. Because of its long lifetime and the resolution of our global simulations ($2° \times 2.5°$), we estimate the contribution of C_2H_6 fossil fuel sources to the global burden and surface mixing ratios of O_3 and PAN rather than focus on specific oil and gas-producing regions. Our estimate is based on the comparison of a simulation without fossil fuel sources of C_2H_6 to the results produced by using 2010 C_2H_6 emissions. The global contribution of fossil fuel C_2H_6 emissions to O_3 and PAN surface mixing ratios has a strong interhemispheric gradient. Due to the C_2H_6 lifetime, which allows its transport to remote areas, the largest impacts on surface O_3 and PAN occur over regions with low emissions of highly reactive hydrocarbons (Figures S2 and S3). The highest impacts on O_3 and PAN surface concentrations occur over the Northern Hemisphere. For O_3, the highest contribution of fossil fuel C_2H_6 emissions to surface mixing ratios is 0.58 ppbv during spring and summertime. Over land areas of the midlatitude Northern Hemisphere, fossil fuel C_2H_6 emissions increase annual average O_3 mixing ratios at the surface by 0.4 ppbv (~1%). The effect is slightly smaller (0.3 ppbv) from 50° to 70°N. For PAN, the highest contributions to surface mixing ratios occur during spring (up to 30 pptv). Fossil fuel C_2H_6 emissions enhance midlatitude Northern Hemisphere continental PAN mixing ratios up to 26 pptv, with an average contribution of ~8% at the surface. The impacts of C_2H_6 oxidation on atmospheric mixing ratios of O_3 and PAN in the free troposphere are more homogeneous across all longitudes but similar in magnitude to the impacts near the surface. As C_2H_6 emissions increase due to important fossil fuel sources like oil and natural gas activities, we anticipate greater contributions to both average mixing ratios of O_3 and PAN. Given the similar emission totals between both C_2H_6 emission inventories, our estimated contribution to global PAN annual burden is consistent with the *Fischer et al.* [2014] estimate of 6%, which was based on the *Xiao et al.* [2008] C_2H_6 emission inventory implemented in GEOS-Chem v.9.01.01.

6. Conclusions

Due to recent and significant increases in the atmospheric C_2H_6 burden, revisiting global C_2H_6 emission inventories is needed. We update a global simulation of C_2H_6 in the GEOS-Chem model by implementing a global C_2H_6 emission inventory estimated from CH_4 fluxes derived from satellite observations and a regional U.S. emission inventory derived by adjusting C_2H_6 emissions from the NEI 2011 upward. We contrast two global C_2H_6 emission inventories for the years 2001 and 2010. We show that these C_2H_6 emission inventories have similar emission totals but very different spatial distributions. In particular, the distribution of emissions differs over the U.S., Europe, Russia, and the Middle East. Our 2010 C_2H_6 emission inventory, which includes C_2H_6 emissions from 2010 satellite-derived CH_4 fluxes and adjusted C_2H_6 emissions from NEI 2011, produces C_2H_6 emissions that are systematically larger over intense gas-producing regions and systematically lower over regions with low natural gas production compared to 2001 C_2H_6 emissions. Globally, the fossil fuel C_2H_6 emissions in 2010 decrease by 0.8 Tg compared to 2001. This difference is consistent with the long-term global decline over this period ending in 2009 [*Franco et al.*, 2015; *Helmig et al.*, 2014a].

When compared to a suite of global observations of C_2H_6, the model simulations capture the C_2H_6 seasonal cycle, the interhemispheric and vertical gradients, the surface mixing ratios, and the C_2H_6 columns in most

regions. However, over some intensive natural gas production regions over the U.S., aircraft measurements reveal greater C_2H_6 mixing ratios compared to the model, especially below 2 km. Given the reported strong increasing trend of the C_2H_6 atmospheric burden that started in 2009 [*Franco et al.*, 2015; *Helmig et al.*, 2016] and an estimated increase of anthropogenic emissions in North America of 75% from 2008 to 2014 [*Franco et al.*, 2016], one plausible reason for this discrepancy could be the time difference between the measurements (2013–2014) and the 2010 C_2H_6 emissions implemented in the model. For these potentially fast-changing emission areas, large assumptions of continental or nationwide C_2H_6/CH_4 emission ratios or emission inventory scaling are not likely to accurately represent the amount, distribution, and mixing ratio impacts of major local sources. Due to the limited observations and the scarcity of long-term in situ C_2H_6 measurements within or downwind of oil and natural gas-producing regions, we recommend the use of different approaches to estimate C_2H_6 emissions for a particular region/basin depending on the type of data available (CH_4/C_2H_6 enhancement ratios, natural gas composition, etc.).

We found that fossil fuel C_2H_6 emissions make the largest contributions to O_3 and PAN over remote areas without large emissions of highly reactive hydrocarbons. Over continental areas in the Northern Hemisphere, we estimate an average increase of ~1% and ~8% to mean annual O_3 and PAN surface mixing ratios, respectively, due to fossil fuel C_2H_6 emissions. On a global scale, these results appear to be largely insensitive to the distribution of C_2H_6 emissions over North America. These contributions from C_2H_6 oxidation to O_3 and PAN abundance are expected to be greater in 2014 compared to 2010 due to increased emissions from oil and natural gas extraction over the U.S. over this period [*U.S. Environmental Protection Agency*, 2015].

References

Aikin, A. C., J. R. Herman, E. J. Maier, and C. J. McQuillan (1982), Atmospheric chemistry of ethane and ethylene, *J. Geophys. Res.*, *87*(C4), 3105, doi:10.1029/JC087iC04p03105.

Akagi, S. K., R. J. Yokelson, C. Wiedinmyer, M. J. Alvarado, J. S. Reid, T. Karl, J. D. Crounse, and P. O. Wennberg (2011), Emission factors for open and domestic biomass burning for use in atmospheric models, *Atmos. Chem. Phys.*, *11*(9), 4039–4072, doi:10.5194/acp-11-4039-2011.

Atkinson, R. (1991), Kinetics and mechanisms of the gas-phase reactions of the NO_3 radical with organic compounds, *J. Phys. Chem.*, *20*(3), 459–507.

Atkinson, R., D. L. Baulch, R. A. Cox, J. N. Crowley, R. F. Hampson, R. G. Hynes, M. E. Jenkin, M. J. Rossi, J. Troe, and I. Subcommittee (2004), Evaluated kinetic and photochemical data for atmospheric chemistry: Volume II—Gas phase reactions of organic species, *Atmos. Chem. Phys.*, *6*, 3625–4055.

Aydin, M., K. R. Verhulst, E. S. Saltzman, M. O. Battle, S. A. Montzka, D. R. Blake, Q. Tang, and M. J. Prather (2011), Recent decreases in fossil-fuel emissions of ethane and methane derived from firn air, *Nature*, *476*(7359), 198–201, doi:10.1038/nature10352.

Barletta, B., S. Meinardi, F. Sherwood Rowland, C.-Y. Chan, X. Wang, S. Zou, L. Yin Chan, and D. R. Blake (2005), Volatile organic compounds in 43 Chinese cities, *Atmos. Environ.*, *39*(32), 5979–5990, doi:10.1016/j.atmosenv.2005.06.029.

Bey, I., D. J. Jacob, R. M. Yantosca, J. A. Logan, B. D. Field, A. M. Fiore, Q. Li, H. Y. Liu, L. J. Mickley, and M. G. Schultz (2001), Global modeling of tropospheric chemistry with assimilated meteorology: Model description and evaluation, *J. Geophys. Res.*, *106*(D19), 23,073, doi:10.1029/2001JD000807.

Blake, D. R., and F. S. Rowland (1986), Global atmospheric concentrations and source strength of ethane, *Nature*, *321*(3), 231–233.

Blake, N. J., et al. (2014), Spatial distributions and source characterization of trace organic gases during SEAC4RS and comparison to DC3, paper presented at 2014 Fall Meeting, AGU, San Francisco, Calif.

Blumenstock, T., F. Hase, I. Kramer, S. Mikuteit, H. Fischer, F. Goutail, and U. Raffalski (2009), Winter to winter variability of chlorine activation and ozone loss as observed by ground-based FTIR measurements at Kiruna since winter 1993/94, *Int. J. Remote Sens.*, *30*(15–16), 4055–4064, doi:10.1080/01431160902821916.

Brandt, A. R., T. Yeskoo, S. McNally, K. Vafi, H. Cai, and M. Q. Wang (2015), *Energy Intensity and Greenhouse Gas Emissions From Crude Oil Production in the Bakken Formation: Input Data and Analysis Methods*, Energy Syst. Div. Argonne Natl. Lab., Lemont, Ill..

Calvert, J. G., R. G. Derwent, J. J. Orlando, G. S. Tyndall, and T. J. Wallington (2008), *Mechanisms of Atmospheric Oxidation of the Alkanes*, Oxford University Press, USA.

Conder, M. W., and K. A. Lawlor (2014), Production characteristics of liquids-rich resource plays challenge facility design., edited.

Etiope, G., and P. Ciccioli (2009), Earth's degassing: A missing ethane and propane source, *Science*, *323*, 1.

Field, R. A., J. Soltis, M. C. McCarthy, S. Murphy, and D. C. Montague (2015), Influence of oil and gas field operations on spatial and temporal distributions of atmospheric non-methane hydrocarbons and their effect on ozone formation in winter, *Atmos. Chem. Phys.*, *15*(6), 3527–3542, doi:10.5194/acp-15-3527-2015.

Fischer, E. V., D. A. Jaffe, and E. C. Weatherhead (2011), Free tropospheric peroxyacetyl nitrate (PAN) and ozone at Mount Bachelor: Potential causes of variability and timescale for trend detection, *Atmos. Chem. Phys.*, *11*(12), 5641–5654, doi:10.5194/acp-11-5641-2011.

Fischer, E. V., et al. (2014), Atmospheric peroxyacetyl nitrate (PAN): A global budget and source attribution, *Atmos. Chem. Phys.*, *14*(5), 2679–2698, doi:10.5194/acp-14-2679-2014.

Franco, B., et al. (2015), Retrieval of ethane from ground-based FTIR solar spectra using improved spectroscopy: Recent burden increase above Jungfraujoch, *J. Quant. Spectrosc. Radiat. Transfer*, *160*, 36–49, doi:10.1016/j.jqsrt.2015.03.017.

Franco, B., et al. (2016), Evaluating ethane and methane emissions associated with the development of oil and natural gas extraction in North America, *Environ. Res. Lett.*, *11*(4044010), doi:10.1088/1748-9326/11/4/044010.

Fung, I., J. John, J. Lerner, E. Matthews, M. J. Prather, L. P. Steele, and P. J. Fraser (1991), Three-dimensional model synthesis of the global methane cycle, *J. Geophys. Res.*, *96*, 13,033–13,065, doi:10.1029/91JD01247.

García, O. E., M. Schneider, A. Redondas, Y. González, F. Hase, T. Blumenstock, and E. Sepúlveda (2012), Investigating the long-term evolution of subtropical ozone profiles applying ground-based FTIR spectrometry, *Atmos. Meas. Tech.*, *5*(11), 2917–2931, doi:10.5194/amt-5-2917-2012.

Ghandi, A., S. Yeh, A. R. Brandt, K. Vafi, H. Cai, M. Q. Wang, B. R. Scanlon, and R. C. Reedy (2015), *Energy Intensity and Greenhouse Gas Emissions From Crude Oil Production in the Eagle Ford Region: Input Data and Analysis Methods*, Inst. of Transp. Stud., Univ. of Calif., Davis.

Gilman, J. B., B. M. Lerner, W. C. Kuster, and J. A. de Gouw (2013), Source signature of volatile organic compounds from oil and natural gas operations in northeastern Colorado, *Environ. Sci. Technol.*, *47*(3), 1297–1305, doi:10.1021/es304119a.

Gupta, M. L., R. J. Cicerone, D. R. Blake, F. S. Rowland, and I. S. A. Isaksen (1998), Global atmospheric distributions and source strengths of light hydrocarbons and tetrachloroethene, *J. Geophys. Res.*, *103*(D21), 28,219–28,235, doi:10.1029/98JD02645.

Hannigan, J. W., M. T. Coffey, and A. Goldman (2009), Semiautonomous FTS observation system for remote sensing of stratospheric and tropospheric gases, *J. Atmos. Oceanic Tech.*, *26*(9), 1814–1828, doi:10.1175/2009jtecha1230.1.

Helmig, D., et al. (2014a), Reconstruction of Northern Hemisphere 1950–2010 atmospheric non-methane hydrocarbons, *Atmos. Chem. Phys.*, *14*(3), 1463–1483, doi:10.5194/acp-14-1463-2014.

Helmig, D., C. R. Thompson, J. Evans, P. Boylan, J. Hueber, and J. H. Park (2014b), Highly elevated atmospheric levels of volatile organic compounds in the Uintah Basin, Utah, *Environ. Sci. Technol.*, *48*(9), 4707–4715, doi:10.1021/es405046r.

Helmig, D., et al. (2016), Reversal of global atmospheric ethane and propane trends largely due to US oil and natural gas production, *Nat. Geosci.*, *9*, 490–495, doi:10.1038/ngeo2721.

Kanakidou, M., H. B. Singh, K. M. Valentin, and P. J. Crutzen (1991), A two-dimensional study of ethane and propane oxidation in the troposphere, *J. Geophys. Res.*, *96*, 15,395–315,413, doi:10.1029/91JD01345.

Kang, M., C. M. Kanno, M. C. Reid, X. Zhang, D. L. Mauzerall, M. A. Celia, Y. Chen, and T. C. Onstott (2014), Direct measurements of methane emissions from abandoned oil and gas wells in Pennsylvania, *Proc. Natl. Acad. Sci. U. S. A.*, *111*(51), 18,173–18,177, doi:10.1073/pnas.1408315111.

Katzenstein, A. S., L. A. Doezema, I. J. Simpson, D. R. Blake, and F. S. Rowland (2003), Extensive regional atmospheric hydrocarbon pollution in the southwestern United States, *Proc. Natl. Acad. Sci. U. S. A.*, *100*(21), 11,975–11,979, doi:10.1073/pnas.1635258100.

Keller, C. A., M. S. Long, R. M. Yantosca, A. M. Da Silva, S. Pawson, and D. J. Jacob (2014), HEMCO v1.0: A versatile, ESMF-compliant component for calculating emissions in atmospheric models, *Geosci. Model Dev.*, *7*(4), 1409–1417, doi:10.5194/gmd-7-1409-2014.

Kohlhepp, R., S. Barthlott, T. Blumenstock, F. Hase, I. Kaiser, U. Raffalski, and R. Ruhnke (2011), Trends of HCl, ClONO$_2$, and HF column abundances from ground-based FTIR measurements in Kiruna (Sweden) in comparison with KASIMA model calculations, *Atmos. Chem. Phys.*, *11*(10), 4669–4677, doi:10.5194/acp-11-4669-2011.

Kort, E. A., M. L. Smith, L. T. Murray, A. Gvakharia, A. R. Brandt, J. Peischl, T. B. Ryerson, C. Sweeney, and K. Travis (2016), Fugitive emissions from the Bakken shale illustrate role of shale production in global ethane shift, *Geophys. Res. Lett.*, *43*, 4617–4623, doi:10.1002/2016gl068703.

Koss, A. R., et al. (2015), Photochemical aging of volatile organic compounds associated with oil and natural gas extraction in the Uintah Basin, UT, during a wintertime ozone formation event, *Atmos. Chem. Phys.*, *15*(10), 5727–5741, doi:10.5194/acp-15-5727-2015.

McKain, K., et al. (2015), Methane emissions from natural gas infrastructure and use in the urban region of Boston, Massachusetts, *Proc. Natl. Acad. Sci. U. S. A.*, *112*(7), 1941–1946, doi:10.1073/pnas.1416261112.

Naik, V., et al. (2013), Preindustrial to present-day changes in tropospheric hydroxyl radical and methane lifetime from the Atmospheric Chemistry and Climate Model Intercomparison Project (ACCMIP), *Atmos. Chem. Phys.*, *13*(10), 5277–5298, doi:10.5194/acp-13-5277-2013.

Olivier, J. G. J. (2002), *On the Quality of Global Emission Inventories. Approaches, Methodologies, Input Data, and Uncertainties*, Utrecht Univ., Netherlands.

Pacsi, A. P., Y. Kimura, G. McGaughey, E. C. McDonald-Buller, and D. T. Allen (2015), Regional ozone impacts of increased natural gas use in the Texas power sector and development in the Eagle Ford shale, *Environ. Sci. Technol.*, *49*(6), 3966–3973, doi:10.1021/es5055012.

Parker, R., et al. (2011), Methane observations from the Greenhouse Gases Observing SATellite: Comparison to ground-based TCCON data and model calculations, *Geophys. Res. Lett.*, *38*, L15807, doi:10.1029/2011GL047871.

Parrella, J. P., et al. (2012), Tropospheric bromine chemistry: Implications for present and pre-industrial ozone and mercury, *Atmos. Chem. Phys.*, *12*(15), 6723–6740, doi:10.5194/acp-12-6723-2012.

Peischl, J., et al. (2015a), Quantification of methane emissions from oil and natural gas extraction regions in the Central/Western U.S. and comparison to previous studies, paper presented at 2015 Fall Meeting, AGU, San Francisco, Calif.

Peischl, J., et al. (2015b), Quantifying atmospheric methane emissions from the Haynesville, Fayetteville, and northeastern Marcellus shale gas production regions, *J. Geophys. Res. Atmos.*, *120*, 2119–2139, doi:10.1002/2014JD022697.

Peischl, J., et al. (2016), Quantifying atmospheric methane emissions from oil and natural gas production in the Bakken shale region of North Dakota, *J. Geophys. Res. Atmos.*, *121*, 6101–6111, doi:10.1002/2015jd024631.

Pekney, N. J., G. Veloski, M. Reeder, J. Tamilia, E. Rupp, and A. Wetzel (2014), Measurement of atmospheric pollutants associated with oil and natural gas exploration and production activity in Pennsylvania's Allegheny National Forest, *J. Air Waste Manage. Assoc.*, *64*(9), 1062–1072, doi:10.1080/10962247.2014.897270.

Pétron, G., et al. (2012), Hydrocarbon emissions characterization in the Colorado Front Range: A pilot study, *J. Geophys. Res.*, *117*, D04304, doi:10.1029/2011JD016360.

Pétron, G., et al. (2014), A new look at methane and nonmethane hydrocarbon emissions from oil and natural gas operations in the Colorado Denver-Julesburg Basin, *J. Geophys. Res. Atmos.*, *121*, 6836–6852, doi:10.1002/2013JD021272.

Plass-Dülmer, C., R. Koppmann, M. Ratte, and J. Rudolph (1995), Light nonmethane hydrocarbons in seawater, *Global Biogeochem. Cycles*, *9*, 79–100, doi:10.1029/94GB02416.

Pozzer, A., J. Pollmann, D. Taraborrelli, P. Jöckel, D. Helmig, P. Tans, J. Hueber, and J. Lelieveld (2010), Observed and simulated global distribution and budget of atmospheric C2–C5 alkanes, *Atmos. Chem. Phys.*, *10*(9), 4403–4422, doi:10.5194/acp-10-4403-2010.

Prather, M. J., C. D. Holmes, and J. Hsu (2012), Reactive greenhouse gas scenarios: Systematic exploration of uncertainties and the role of atmospheric chemistry, *Geophys. Res. Lett.*, *39*, L09803, doi:10.1029/2012GL051440.

Prinn, R. G., et al. (2005), Evidence for variability of atmospheric hydroxyl radicals over the past quarter century, *Geophys. Res. Lett.*, *32* L07809, doi:10.1029/2004GL022228.

Randerson, J. T., Y. Chen, G. R. van der Werf, B. M. Rogers, and D. C. Morton (2012), Global burned area and biomass burning emissions from small fires, *J. Geophys. Res.*, *117*, G04012, doi:10.1029/2012JG002128.

Richter, D., P. Weibring, J. G. Walega, A. Fried, S. M. Spuler, and M. S. Taubman (2015), Compact highly sensitive multi-species airborne mid-IR spectrometer, *Appl. Phys. B*, *119*(1), 119–131, doi:10.1007/s00340-015-6038-8.

Roscioli, J. R., et al. (2015), Measurements of methane emissions from natural gas gathering facilities and processing plants: Measurement methods, *Atmos. Meas. Tech.*, *8*(5), 2017–2035, doi:10.5194/amt-8-2017-2015.

Rudolph, J. (1995), The tropospheric distribution and budget of ethane, *J. Geophys. Res.*, *100*(6), 11.

Rudolph, J., and D. H. Ehhalt (1981), Measurements of C2–C5 hydrocarbons over the North Atlantic, *J. Geophys. Res.*, *86*(C12), 11,959, doi:10.1029/JC086iC12p11959.

Sander, S. P., et al. (2003), *Chemical Kinetics and Photochemical Data for Use in Atmospheric Studies, Evaluation No. 14*, edited by J. P. Laboratory, JPL Publ., Pasadena, Calif.

Sander, S. P., et al. (2011), *Chemical Kinetics and Photochemical Data for Use in Atmospheric Studies, Evaluation No. 17*, edited by J. P. Laboratory, JPL Publ., Pasadena, Calif.

Saunois, M., et al. (2016), The global methane budget: 2000–2012, *Earth Syst. Sci. Data Discuss.*, *8*(2), 697–751, doi:10.5194/essd-2016-25.

Schauffler, S. A., et al. (2014), Organic halogen and hydrocarbon distributions during SEAC4RS measured from the ER-2 and DC-8, paper presented 2014 Fall Meeting, AGU, San Francisco, Calif.

Schneider, M., P. M. Romero, F. Hase, T. Blumenstock, E. Cuevas, and R. Ramos (2010), Continuous quality assessment of atmospheric water vapour measurement techniques: FTIR, Cimel, MFRSR, GPS, and Vaisala RS92, *Atmos. Meas. Tech.*, *3*, 323–338.

Schwietzke, S., W. M. Griffin, H. S. Matthews, and L. M. Bruhwiler (2014), Natural gas fugitive emissions rates constrained by global atmospheric methane and ethane, *Environ. Sci. Technol.*, *48*(14), 7714–7722, doi:10.1021/es501204c.

Sherwen, T., et al. (2016), Global impacts of tropospheric halogens (Cl, Br, I) on oxidants and composition in GEOS-Chem, *Atmos. Chem. Phys.*, *16*(18), 12,239–12,271, doi:10.5194/acp-16-12239-2016.

Simpson, I. J., et al. (2010), Characterization of trace gases measured over Alberta oil sands mining operations: 76 speciated C2–C10 volatile organic compounds (VOCs), CO2, CH4, CO, NO, NO2, NOy, O3 and SO2, *Atmos. Chem. Phys.*, *10*(23), 11,931–11,954, doi:10.5194/acp-10-11931-2010.

Simpson, I. J., et al. (2011), Boreal forest fire emissions in fresh Canadian smoke plumes: C1–C10 volatile organic compounds (VOCs), CO2, CO, NO2, NO, HCN and CH3CN, *Atmos. Chem. Phys.*, *11*(13), 6445–6463, doi:10.5194/acp-11-6445-2011.

Simpson, I. J., M. P. Sulbaek Andersen, S. Meinardi, L. Bruhwiler, N. J. Blake, D. Helmig, F. S. Rowland, and D. R. Blake (2012), Long-term decline of global atmospheric ethane concentrations and implications for methane, *Nature*, *488*(7412), 490–494, doi:10.1038/nature11342.

Singh, H. B., and P. B. Zimmerman (1992), Atmospheric distribution and sources of nonmethane hydrocarbons, in *Gaseous Pollutants: Characterization and Cycling*, edited by J. O. Nriagu, pp. 177–235, Wiley, New York.

Speight, J. G. (2013), *Shale Gas Properties and Processing*, pp. i–iii, Gulf Prof., Boston.

Swarthout, R. F., R. S. Russo, Y. Zhou, A. H. Hart, and B. C. Sive (2013), Volatile organic compound distributions during the NACHTT campaign at the Boulder Atmospheric Observatory: Influence of urban and natural gas sources, *J. Geophys. Res. Atmos.*, *118*, 10,614–10,637, doi:10.1002/jgrd.50722.

Thompson, C. R., J. Hueber, and D. Helmig (2014), Influence of oil and gas emissions on ambient atmospheric non-methane hydrocarbons in residential areas of Northeastern Colorado, *Elementa*, *2*(000035), 1–17, doi:10.12952/journal.elementa.000035.

Turner, A. J., and D. J. Jacob (2015), Balancing aggregation and smoothing errors in inverse models, *Atmos. Chem. Phys.*, *15*(12), 7039–7048, doi:10.5194/acp-15-7039-2015.

Turner, A. J., et al. (2015), Estimating global and North American methane emissions with high spatial resolution using GOSAT satellite data, *Atmos. Chem. Phys.*, *15*(12), 7049–7069, doi:10.5194/acp-15-7049-2015.

U.S. Environmental Protection Agency (2013), National Emissions Inventory 2011, version 1, edited by E. P. Agency.

U.S. Environmental Protection Agency (2015), Drilling Productivity Report for key tight oil and shale gas regions.

van der Werf, G. R., J. T. Randerson, L. Giglio, G. J. Collatz, M. Mu, P. S. Kasibhatla, D. C. Morton, R. S. DeFries, Y. Jin, and T. T. van Leeuwen (2010), Global fire emissions and the contribution of deforestation, savanna, forest, agricultural, and peat fires (1997–2009), *Atmos. Chem. Phys.*, *10*(23), 11,707–11,735, doi:10.5194/acp-10-11707-2010.

Vinciguerra, T., S. Yao, J. Dadzie, A. Chittams, T. Deskins, S. Ehrman, and R. R. Dickerson (2015), Regional air quality impacts of hydraulic fracturing and shale natural gas activity: Evidence from ambient VOC observations, *Atmos. Environ.*, *110*, 144–150, doi:10.1016/j.atmosenv.2015.03.056.

Wang, J. S., J. A. Logan, M. B. McElroy, B. N. Duncan, I. A. Megretskaia, and R. M. Yantosca (2004), A 3-D model analysis of the slowdown and interannual variability in the methane growth rate from 1988 to 1997, *Global Biogeochem. Cycles*, *18*, GB3011, doi:10.1029/2003GB002180.

Warneke, C., et al. (2014), Volatile organic compound emissions from the oil and natural gas industry in the Uintah Basin, Utah: Oil and gas well pad emissions compared to ambient air composition, *Atmos. Chem. Phys.*, *14*, 10,977–10,988, doi:10.5194/acp-14-10977-2014.

Wiacek, A., J. R. Taylor, K. Strong, R. Saari, T. E. Kerzenmacher, N. B. Jones, and D. W. T. Griffith (2007), Ground-based solar absorption FTIR spectroscopy: Characterization of retrievals and first results from a novel optical design instrument at a new NDACC complementary station, *J. Atmos. Oceanic Tech.*, *24*(3), 432–448, doi:10.1175/jtech1962.1.

Wofsy, S. C., et al. (2012), *HIPPO Combined Discrete Flask and GC Sample GHG, Halo-, Hydrocarbon Data (R_20121129)*, edited by O. R. N. L. Carbon Dioxide Inf. Anal. Cent., Oak Ridge, Tenn., doi:10.3334/CDIAC/hippo_012.

Xiao, Y. P., D. J. Jacob, J. S. Wang, J. A. Logan, P. I. Palmer, P. Suntharalingam, R. M. Yantosca, G. W. Sachse, D. R. Blake, and D. G. Streets (2004), Constraints on Asian and European sources of methane from CH4-C2H6-CO correlations in Asian outflow, *J. Geophys. Res.*, *109*, D15S16, doi:10.1029/2003JD004475.

Xiao, Y. P., J. A. Logan, D. J. Jacob, R. C. Hudman, R. M. Yantosca, and D. R. Blake (2008), Global budget of ethane and regional constraints on US sources, *J. Geophys. Res.*, *113*, D21306, doi:10.1029/2007JD009415.

Yacovitch, T. I., and S. C. Herndon (2014), TILDAS ethane quality assurance document, discover AQ Denver 2014.

Yevich, R., and J. A. Logan (2003), An assessment of biofuel use and burning of agricultural waste in the developing world, *Global Biogeochem. Cycles*, *17*(4), 1095, doi:10.1029/2002GB001952.

Zimmerman, P. R., J. P. Greenberg, and C. E. Westberg (1988), Measurements of atmospheric hydrocarbons and biogenic emission fluxes in the Amazon Boundary Layer, *J. Geophys. Res.*, *93*, 1407–1416, doi:10.1029/JD093iD02p01407.